Experimental validation of a lower order model for a flat-plate latent thermal energy storage heat exchanger

Wim Beyne[1,2], Maike Johnson[3], Andrea Gutierrez[3] and Michel De Paepe[1,2,4]

[1] Ghent University, Faculty of Engineering and Architecture, Department of Electrical Energy, Metals, Mechanical Constructions & Systems, Ghent 9000, Belgium

[2] FlandersMake@UGent – Core Lab MIRO, Ghent 9000, Belgium

[3] Institute of Engineering Thermodynamics, German Aerospace Center (DLR), Pfaffenwaldring 38-40, 70569 Stuttgart, Germany

[4] Department of Mechanical Engineering, University of Cape Town, Private Bag X3, Rondebosch 7701, South Africa

Abstract

Latent thermal energy storage systems have seen a large amount of interest from a broad range of applications. Design and sizing of these systems however, remains difficult as finite volume methods are limited by computational resources. Furthermore, classic heat exchanger design methods are not applicable to storage systems as these design methods are based on a steady state analysis. The present paper proposes a computationally efficient modeling method that can deal with both the transient nature of the operation of the storage system and large domain sizes. The model is based on three previously developed separate sub-models, which are connected through a space-series approach. An essential new aspect of this work is the application of the method to a flat-plate latent thermal energy storage heat exchanger, for which a large experimental data set is available, including both melting and solidification experiments. Additionally, the model incorporates heat losses, which were not considered in previous models. The model predictions of the outlet temperature are on average within 1.2 K with the measured outlet temperature with the largest deviations at the start of the (dis)charging and at the end of the phase change. Further research is needed to refine the representation of phase change dynamics and heat losses to improve predictive accuracy. Despite these limitations, the model effectively predicts outlet temperature in most cases, while requiring minimal computational effort. Unlike finite volume methods, its computational cost remains independent of system size.

Keywords Latent thermal energy storage, phase change material, design and sizing experimental

Highlights

- Thermal energy storage system design requires computationally efficient design models.
- A sizing model is developed by combining models for the sensible and latent heat.
- The model predicts the outlet temperature and heat loss of the system.
- The method is tested on a high temperature flat plate storage system.

Graphical abstract

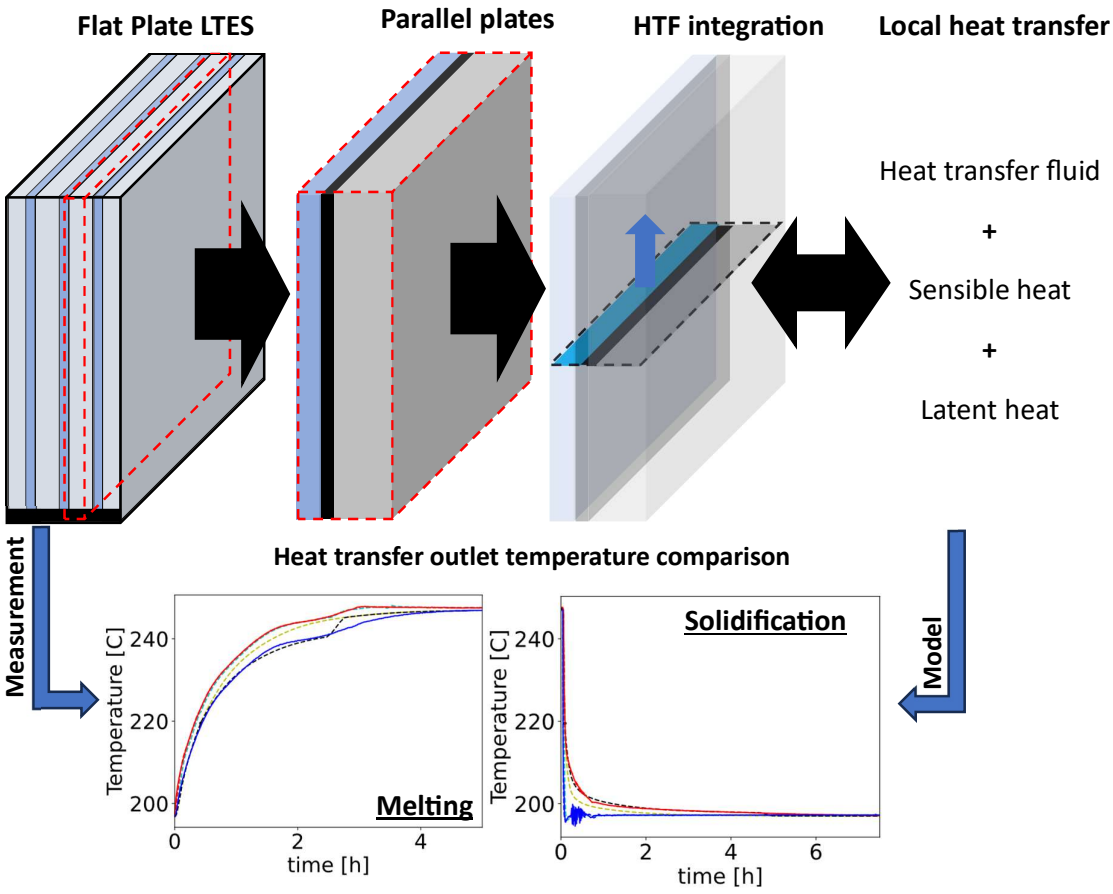

1. Introduction

Energy storage is a key technology in the switch from fossil to renewable energy sources. One type of energy storage is thermal energy storage (TES), where the energy is released in the form of heat [1]. Three types of TES are classically distinguished: sensible, latent and thermochemical energy storage [2]. The distinction between the three types is based on the internal energy change of the storage system: for sensible TES (STES) the internal energy change is related to a temperature change, for latent TES (LTES) it is in the form of latent heat of phase change while for thermochemical TES it is in the form of the chemical energy of a reaction. The present paper focusses specifically on latent thermal energy storage systems.

LTES systems use the latent heat of phase change to increase the energy density of the system compared to STES systems. Fittingly, the storage material in LTES systems is called the phase change material (PCM) where a solid-liquid phase change is most common. PCM's can be found for a wide range of temperatures [2] and for applications such as buildings [3], cold chain transport and storage [4], industrial heat storage [5], solar heating with heat pumps [6] and solar drying [7]. The PCM has to be contained within the TES system. Two types of encapsulation are distinguished: nano- and macro encapsulation depending on the size of the PCM container [2]. Once a PCM and an encapsulation method is chosen, heat has to be transferred to and from the PCM. Commonly, this is done by employing the forced flow of a heat transfer fluid (HTF).

The main key performance indicator for an LTES system with a forced flow of HTF is the outlet state of the HTF for a given inlet state [1]. The present work aims at validating a modeling tool for design of LTES systems and therefore the main objective is to predict the outlet state of the HTF. A second requirement for a design model is to take into account the geometry and size of the system. An overview of some of the design and sizing tools which have been developed in literature is given below.

Computational Fluid Dynamics (CFD) is a useful tool for modeling LTES systems. CFD in LTES systems faces the specific challenge of modeling the solid-liquid phase change. Numerical models for solid liquid phase change can be categorized in two frameworks: front-tracking or multiple domain methods [8] and fixed-grid methods [9, 10]. The front-tracking methods explicitly track the phase change front location and can thus explicitly distinguish between the solid and liquid domain. Although front tracking methods are more accurate for problems with a sharp PCM interface, the methods can be difficult to use in complex geometries due to the requirement of modifying the mesh as the solid-liquid interface moves. As LTES systems often have complex finned geometries (e.g. bifurcated longitudinal fins [11]), fixed-grid methods and specifically the enthalpy-porosity method has become the dominant method for CFD in LTES systems [12].

The enthalpy porosity method is limited by the required number of nodes and the time step size. A review of recent papers on modeling solid liquid phase change using the enthalpy porosity found element sizes between 0.8 and 0.08 mm [13-23]. An example of such a study is the work of Vogel et al. [24, 25] which models a finned shell-and-tube LTES heat exchanger. The study focusses on short sections (100 mm) of a single tube, which is surrounded by a tube of PCM with a 230 mm diameter. The tube sections are meshed with a cell size between 0.25 mm and 0.5 mm in the radial direction and 1 mm in the axial direction, which results in a total number of 3 133 053 nodes. The short tubes studied by Vogel et al. [24, 25] are of course not representative of large scale systems with longer tube lengths (e.g. the finned tube studied by Couvreur et al. [5] with a 5.36m tube length). Modeling these larger systems with a state-of-the-art grid resolution is unfeasible due to the resulting number of nodes.

A fully resolved CFD simulation is not feasible for most LTES system of a practical size. In order to still obtain a workable model, the natural convection in the PCM melt is sometimes neglected (e.g. [7, 26-

28]). Neglecting natural convection is often seen as a reasonable assumption in solidification cases [2, 29], however Jmal and Baccar [30] found natural convection to have a significant impact on the HTF outlet temperature of the air-PCM heat exchanger that was studied. For melting, natural convection cannot be neglected. Therefore, the calculation is sometimes simplified using an effective thermal conductivity [31]. Pointner et al. [32] compared different mathematical implementations of the latent heat of phase change in terms of calculation speed and accuracy for a flat plate heat exchanger where the natural convection was modeled as an effective thermal conductivity. The works of Vogel et al. [24, 25] and Couvreur et al. [5] take this approach one step further by also modeling the fins as an effective homogeneous structure. The effective conductivity is fitted based on small scale experiments or CFD simulations and used to predict the behavior of larger systems. These type of models will be referred to as homogeneous diffusion-only models.

Figure 1 shows the necessary steps to obtain a homogeneous diffusion-only model from a full LTES system in the case of a shell-and-tube LTES system. In the first step, the domain is limited where symmetry over the tubes is assumed and an equivalent PCM annulus is assumed around the finned tube. In a second step, a section of the finned tube is modeled in detail and the resulting heat flux and stored energy is mapped to a diffusion-only bare tube by fitting an effective thermal conductivity. Using this effective thermal conductivity, the full tube is simulated as a homogeneous diffusion-only model.

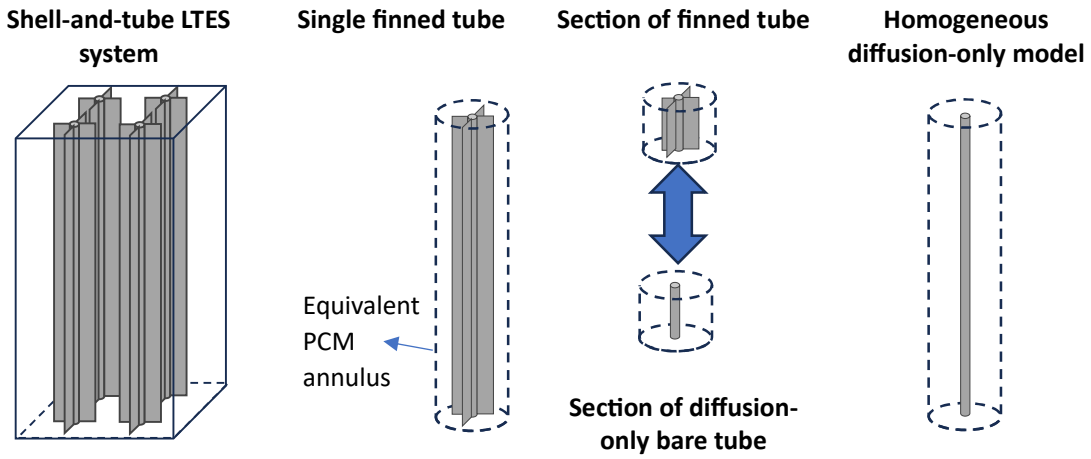

Figure 1: Schematic overview of the steps taken from a shell-and-tube LTES system to a homogeneous diffusion-only model.

The homogeneous diffusion-only approach features characterizing heat transfer in a representative section, mapping this solution to a diffusion-only system, and extrapolating based on an effective thermal conductivity. In recent years, semi-analytical models for both STES [33] and LTES heat exchangers [34, 35] have been developed based on a similar idea. In these models, the local heat transfer is modeled as a relation between the HTF temperature and the heat flux or stored energy as a function of time. This local heat transfer is then integrated over the heat transfer surface area to obtain a sizing model of the system. The advantage of this approach compared to the homogeneous diffusion-only approach is that time stepping or spatial discretization is no longer needed, reducing computational cost and implementation complexity. Furthermore, the approach does not require a mapping to a diffusion-only solution.

The semi-analytical models can model purely sensible TES systems [33] or purely latent heat TES systems [34, 35]. A real LTES system will always have both sensible heat and latent heat changes during charging and discharging. Beyne et al. [36] compared three methods to include both sensible and

latent heat. The first approach included the sensible heat in the latent heat model by artificially increasing the latent heat of phase change. The second approach assumed the heat exchanger to be at a uniform temperature during the initial sensible stage as was done in the work of Ding et al. [37]. This approach is referred to as the time-series approach, since it assumes a sensible stage and a latent stage in the (dis)charging of the LTES system. The third approach separates in space as introduced in [38]: a heat exchanger with only sensible heat is connected to a heat exchanger with only latent heat. This approach is referred to as the space-series approach. For the case studied by Beyne et al. [36], the space-series-approach was found to have the best agreement with experimental data.

There are two remaining gaps in the work of Beyne et al. [36]. First of all, heat losses are not included in the model. Since the studied heat exchanger has significant heat losses, the model predictions deviate from the measured system output especially at the end of charging when heat losses are dominant. The second gap is that the study only contains a single validation melting experiment on a radially finned shell-and-tube LTES heat exchanger.

The present paper applies the modeling method to a flat-plate heat exchanger for which a large set of experimental data is available. This data set includes both melting and solidification cases, in contrast to previously published work. Furthermore, the paper models the heat losses by implementing it into the characterization of the sensible system. The novelty of the paper compared to previous work [36] is thus the inclusion of heat losses and the extensive validation for both melting and solidification cases.

The motivation for this type of model arises from the limitations of existing modeling tools for LTES systems. Computational Fluid Dynamics (CFD) approaches, while detailed, become impractical for large-scale systems due to their immense computational cost; in contrast, the proposed model maintains a computational complexity that does not scale with system size. Homogeneous diffusion models rely on time-stepping and spatial discretization, which introduce numerical constraints, whereas the present framework operates without the need for either. Prior analytical models have been limited to either sensible or latent heat, whereas this study integrates both. As stated above, existing hybrid analytical models often neglect heat losses and lack experimental validation; the proposed approach overcomes these gaps by explicitly incorporating heat losses and undergoing extensive validation across a wide experimental dataset. This work thus provides a robust, efficient, and experimentally validated modeling framework for LTES systems.

The method of the present paper is validating the modeling approach by comparing the outlet temperature predictions to measured outlet temperature. In the next section, the experimental setup is introduced together with the experimental procedure. The following section discusses the heat exchanger model which includes a model for the heat transfer fluid, the sensible heat and the latent heat. The fourth section discusses and analyzes the experimental results and compares the outlet temperature prediction of the model to the experimentally measured temperatures. Based on the results, the advantages, limitations and future recommendations are discussed.

2. Experimental setup description

A flat plate heat storage unit conceived as an adaptation of the flat plate heat exchanger [39] is shown in Figure 2 schematically and as-built in Figure 3. The testing of the unit was described in [40]. The unit is comprised of four PCM chambers open to the atmosphere separated by three HTF flow chambers. The two inner, wider PCM chambers are for analysis and two outer, smaller PCM chambers to reduce environmental heat loss. The storage system was designed for heat storage operating on molten salts with thermal oil as heat transfer fluid.

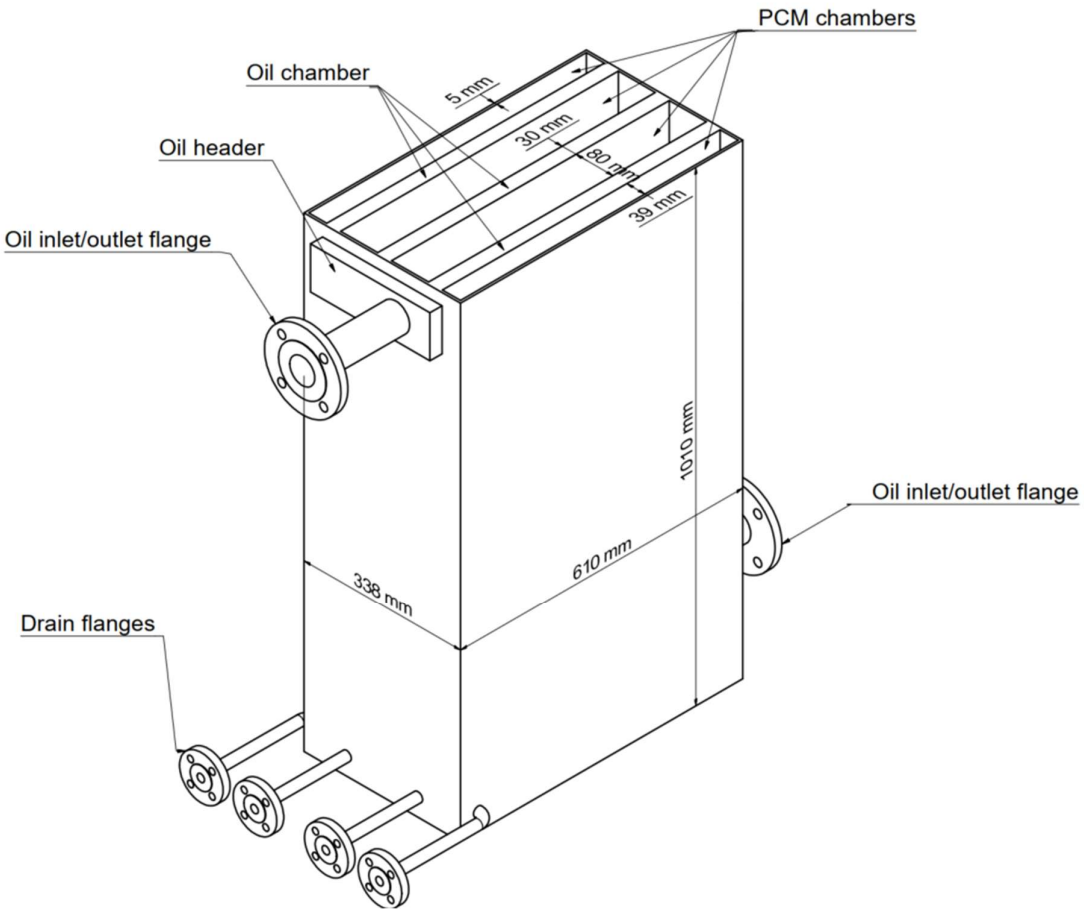

Figure 2: Experimental storage unit in a flat plate heat exchanger design that consists of heat transfer fluid (HTF) chambers and phase change material (PCM) enclosures. The HTF flows downwards while charging and upwards while discharging and is connected to the testing system by two flanges [40].

Figure 3: Experimental storage unit in a flat plate heat exchanger, insulated and integrated in testing loop [40].

This storage unit is designed for operating temperatures up to 300 °C and is made of carbon steel 1.0425 (material properties given in Table 3). In order to withstand the pressures in the HTF system, metal rods are welded to both the left and right sides of each HTF chamber. Each of the chambers is stiffened with 27 rods. This design resulted in a steel mass of about 220 kg.

Table 1: Relevant Steel 1.0425 properties [41].

Property		Error
Specific heat capacity	540 J/kgK	± 0.5 J/kgK
Thermal conductivity	51 W/mK	± 0.5 W/mK
Density	1959 kg/m³	± 0.5 kg/m³

The wider PCM chambers are about 8 cm wide and filled with a eutectic mixture of KNO_3-$NaNO_3$ (material properties given in Table 1). These wide chambers allow for modifications to the storage design by use of heat transfer structures, as discussed in [42]. The total PCM mass was about 250 kg. The technical grade salt used in this storage had a melting temperature onset of 219.5 °C. This storage unit filled with this salt has a latent heat capacity of approximately 7.5 kWh.

The properties for the PCM are assumed constant as was done in a prior numerical study on this system [41] (Table 2). The error estimates are based on the reported significant figures. The density of the PCM is calculated as the total weight of PCM in the system divided by the total volume of the PCM. The use of this effective density does not take the volume change of the PCM into account however it does ensure that the total mass of PCM is the same in the model as in LTES heat exchanger, which reduces the error made on the energy balance of the system.

Table 2: Relevant PCM properties [41].

Property		Error
Melting temperature	219.5 °C	± 0.05 °C
Latent heat	94 kJ/kg	± 0.5 J/kg
Specific heat capacity liquid	1492 J/kgK	± 0.5 J/kgK
Specific heat capacity solid	1350 J/kgK	± 0.5 J/kgK
Thermal conductivity	0.435 W/mK	± 0.0005 W/mK

The HTF used in this test loop is Mobiltherm 603 (properties given in Table 2). The heating power is 12 kW and the cooling power is 30 kW. The maximum flow rate in the test loop is 3 m³/h and the feasible temperature range is 20-300 °C. Through a valve bypass connection, it is possible to change the flow direction within the storage unit, so that the storage can be charged with one flow direction and discharged with the other. The storage unit is contained in a secondary oil container in case of leaks, and insulated on all sides. The insulation has a thickness of 25 cm, material properties are given in Table 4. The test loop is controlled by a SPS unit from Siemens and data is stored at a 10 s interval.

The HTF is modeled as a single-phase incompressible fluid with a constant specific heat capacity. The manufacturer provides the density, specific heat capacity, thermal conductivity and kinematic viscosity as a function of temperature. Of these properties, only the density and specific heat capacity are used in the present model as the convective heat transfer coefficient is determined as 200 W/m²K from a previous study on this geometry [41]. The values for density and specific heat capacity are determined at the average of the initial and HTF inlet temperature for each test. In order to estimate the effect of this simplification, Table 3 reports the density and specific heat capacity as well as the product of those properties at the PCM phase change temperature. The variation of the properties within the tested temperature range is reported in the last column. The maximal error on the product of density and specific heat is 1.2%.

Table 3: Mobiltherm 603 property values and variation in the experimental testing range.

Property	At T_{pc}=219.5 °C	% variation ± 25 °C
Density	728.1 kg/m³	± 2.3%
Specific heat capacity	2.620 kJ/kgK	± 3.5%
Density*Specific heat capacity	1908 kJ/m³K	± 1.2%

Appendix A gives an estimation of the impact of the material properties uncertainty on the energy balance and heat transfer rate. The resulting error for the energy balance is only 0.7% while the error on the average heat transfer rate is about 0.1% mostly due to the error on the thermal conductivity of the PCM.

The system is insulated with 250 cm of mineral wool on all sides except the bottom. The bottom is insulated with 25 cm of a Contherm MP 1000 insulating plate and 200 mm of calcium silicate plate. The thermal conductivity of each of these materials is given in Table 4.

Table 4: Insulation material properties.

Thermal conductivity [W/mK]	Temperature				
Material	200 °C	250 °C	300 °C	350 °C	400 °C
CONTHERM MP 1000	0,02				0,024
Mineral Wool	0,064	0,076	0,090	0,106	0,123
Calcium Silicate plate	0,076	0,08	0,087	0,094	0,101

Various data points are measured in the test loop. These include the temperature of the HTF at the inlet and outlet of the storage unit via Pt-100 resistance thermometers, the differential pressure and volumetric flow rate in the HTF system, and the temperature in the PCM at various points via type K thermocouples. Calibration of the thermocouples showed a temperature difference of about 0.92 °C. This is within the error range of the thermocouples (minimum 1.5 °C) in this temperature range. The error estimates for the measurement equipment used in this work are summarized in Table 5.

Table 5: Error estimates for measurement equipment used in the analysis in this work.

Quantity	Measurement device	Measurement error
HTF temperature difference	Pt-100	± 0.92 °C
Temperature	Pt-100 and thermocouple	± 1.5 °C
Volume flow rate	Optimass 9000 S15	0.1% of the measured value

The temperature distribution of the HTF within the oil chambers can only be approximately measured by measuring the wall temperature on the PCM-chamber-side of the steel and calculating the approximate difference. In order to understand the flow in the oil chambers, thermocouples were clamped over the face of the steel plate to the oil chambers and the temperatures measured during heating and cooling of the oil in the HTF system prior to the PCM filling of the storage. These experiments showed a low temperature deviation from the left to right in the oil chambers (below 1 K) and the temperature deviation between the three oil chambers shown by differing average temperatures over time was between 1 to 1.5 K at 2 m³/h.

In order to understand the storage characteristics, the volumetric flow rate of the HTF and the temperature range about the melting temperature of the PCM were varied. A full parametric variation of the following two parameter variations was completed.

- Temperature range: ±10 K, ±18 K, ±25 K
- Volumetric flow rate: 0.5 m³/h, 2 m³/h

For discharging experiments, the storage unit is heated to the set temperature above the melting temperature and the mass flow rate set in the controls. To begin the testing, the discharging temperature is set in the HTF and this was attained during circulation through the system. Discharging is continued until a uniform temperature is attained. For charging, the opposite order is used – storage unit is cooled to the set temperature below the melting temperature of the PCM to have a uniform temperature. The test loop is set to the mass flow rate and charging temperature. As the charging power of the test loop is lower than that of the cooling loop, and heat losses further reduce this power, attaining the charging temperature in the HTF takes longer than for discharging processes. Charging continues until a uniform temperature in the unit is attained, well beyond melting of the PCM is completed.

3. Heat exchanger model

Consider a latent storage system with a single-phase heat transfer fluid (HTF) as depicted in Figure 4. There are two major key performance indicators: the outlet state and mass flow rate of the HTF and the heat losses to the environment as these are the only interaction the system has with its environment [1]. Both of these KPI's should be determined as a function of the HTF inlet state, the system initial condition and time.

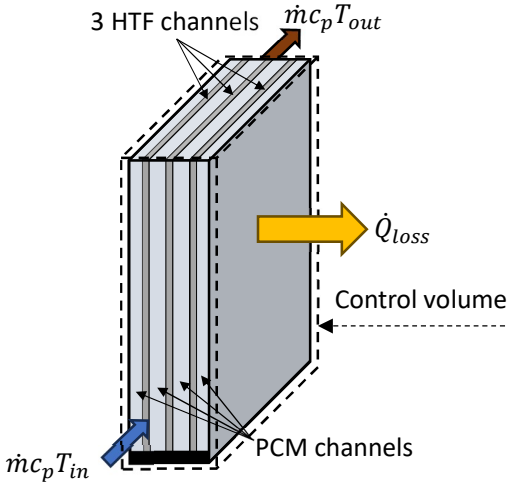

Figure 4: Schematic depiction of the flat-plate LTES system with marked inlet, outlet and heat losses.

The external KPI's of the system can be linked to each other and the internal state of the system by applying the conservation of energy on the control volume depicted in Figure 4. The conservation of energy results in Equation (1).

$$\dot{m}(h_{out} - h_{in}) = \frac{dU}{dt} - \dot{Q}_{loss} \quad (1)$$

With
- $\dot{m}$ the mass flow rate of the HTF
- h_{out}, h_{in} Respectively the out- and inlet enthalpy of the HTF
- U The internal energy of the storage system
- $\dot{Q}_{loss}$ The heat losses from the system to the environment

Equation (1) connects the outlet state of the HTF (h_{out}) with the inlet condition (h_{in} and $\dot{m}$), the heat loss and the state of the system (U). A model for the state of the system can thus be used to predict the output of the system.

Equation (1) is generally valid for storage systems with a single-phase heat transfer fluid. In order to derive a model, several simplifications will be introduced, which can be grouped into four categories: material properties, geometry, sensible and latent heat decomposition and the space-series approach. Each category is explained in the following sub-sections.

3.1. Geometry: the parallel channel assumption

The flat-plate LTES system features 3 HTF channels and four PCM volumes. This geometry can be simplified as 6 parallel HTF channels with 1/6 of the total PCM and separated by a metal wall. The HTF has an inlet and outlet at respectively the lower and upper surface as well as a symmetrical boundary condition on the lefthand side of the system. Losses are assumed to occur at the righthand side area of the PCM while all other outside sides of the container and PCM are assumed to be adiabatic.

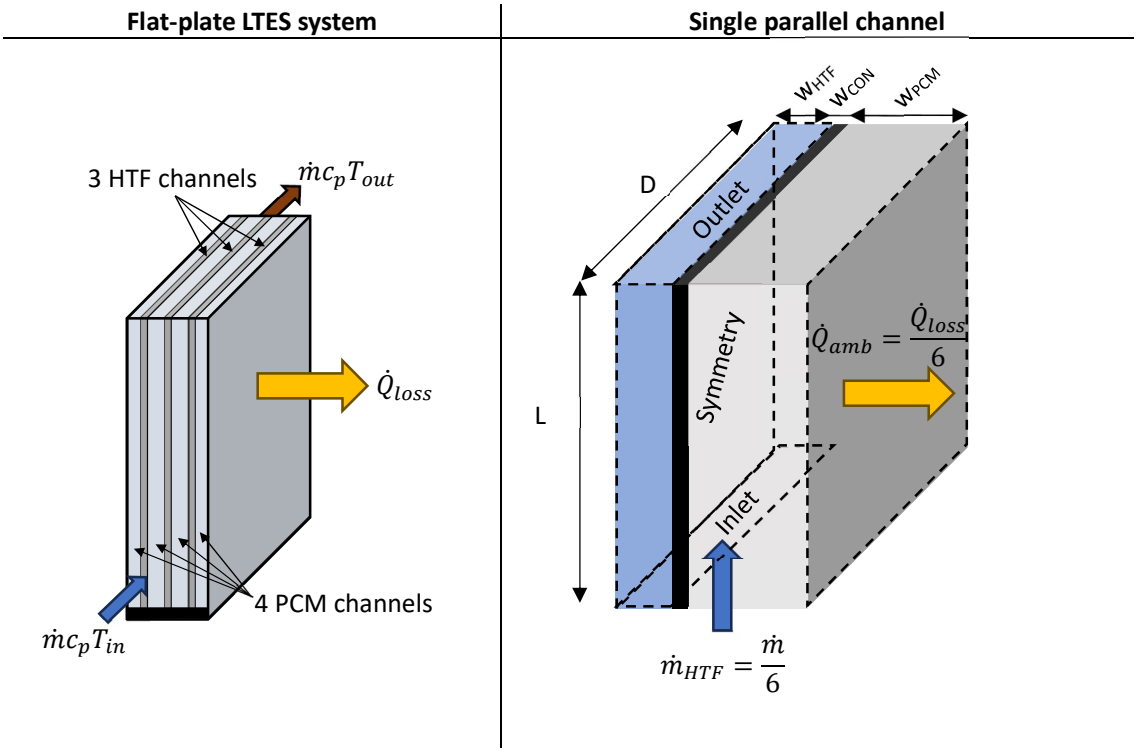

Figure 5: Schematic depiction of the flat-plate LTES system and the single parallel channel simplification with marked inlet, outlet and faces with heat loss. All non-marked sides are adiabatic.

As discussed in the introduction, assuming parallel identical channels is a common strategy when modelling LTES systems (see e.g. [43]). This approach was also taken in a previous CFD study of the flat-plate geometry [41]. However, it is important to stress the simplifications inherent to this approach.

A first simplification is assuming parallel identical channels, which is not the case due to the heat losses and the possible inequal HTF distribution. There is no measurement on the distribution of the HTF and therefore the equal distribution assumption is a reasonable assumption. The heat losses occur on the outer surfaces of the system, while the single parallel channel assumes the losses to occur on the outer side of the system.

A second simplification concerns the HTF inlet and outlet. The flat-plate system has an inlet on the front near the bottom of the system and an outlet on the back near the top of the system. As described by Vogel et al. [41], the flow of the HTF is vertical in the middle section of the heat exchanger. The exact flow patterns in the inlet and outlet of the system are not included in the model.

A final simplification is the absence of the metal container on the bottom, top and sides of the HTF and PCM channels. These metal sides can act as fins and thus have an effect on the heat transfer to the storage material. However, this effect is neglected in the lower order modelling presented in this paper.

The simplifications of the parallel channel assumption will lead to a modelling error. In terms of the energy equation (Equation (1)), two errors can be distinguished: an error in the heat transfer rate and an error in the overall internal energy change of the system. In order to avoid the latter of these errors, the mass of metal and PCM has to be the same in the parallel channel model as in the flat-plate LTES system. The total mass of metal and PCM is known for the flat-plate LTES system. For the metal mass,

the width of the container wall is increased to match the total mass. For the PCM, an effective PCM density is introduced to match the mass.

3.2. Heat exchanger decomposition

Equation (1) describes the overall energy balance of the system. In order to obtain a local expression of the conservation of energy, the HTF is modeled as plug flow: the state of the HTF is described by the bulk temperature at a constant height (defined by the y-axis in Figure 6). This results in a one-dimensional description of the HTF state $T_{HTF}(y,t)$ (Equation (2)). Similarly, the internal energy of the system can be described as Equation (3) and the heat loss to the ambient as Equation (4).

$$T_{HTF}(y,t) = \frac{1}{D\, w_{HTF}} \int_0^D \int_0^{w_{HTF}} T_{HTF}(x,y,z,t)\, dx\, dz \tag{2}$$

$$U(y,t) = \int_0^D \int_0^W u(x,y,z,t)\, dx\, dz \tag{3}$$

$$\dot{q}_{amb}(y,t) = \int_0^D \dot{q}_{amb}\, dz \tag{4}$$

With

D	Total size of the single parallel plate in the z-direction
W	Total size of the single parallel plate in the x-direction
w_{HTF}	Width of the HTF layer
$u(x,y,z,t)$	The local specific internal energy

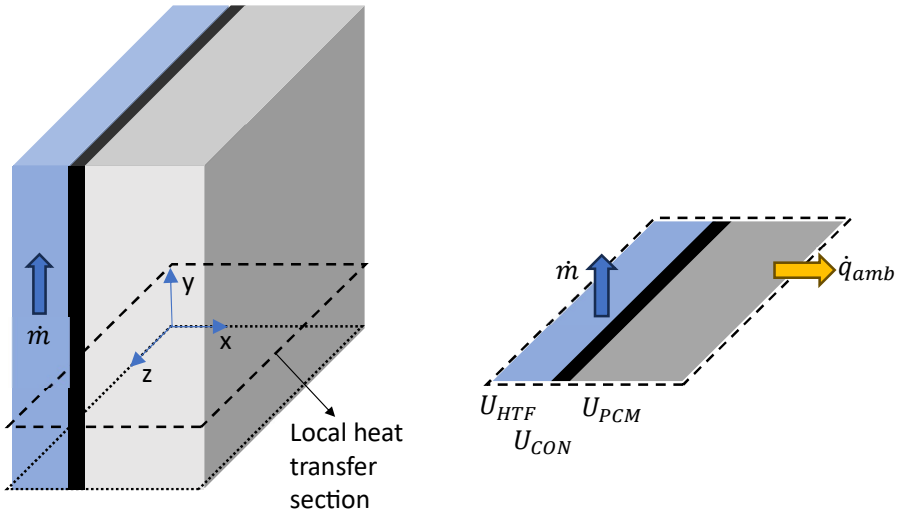

Figure 6: The single parallel channel simplification with the local surface area *A* and local heat transfer section highlighted.

Figure 6 highlights a cross section at the position determined by the y coordinate as the local heat transfer section. Based on the bulk temperature, internal energy and heat loss defined above, the conservation of energy can be written in the local heat transfer section as Equation (5). The inlet and initial condition are expressed by Equation (6) and (7).

$$\dot{m}_{HTF} c_{HTF} \frac{dT_{HTF}(y,t)}{dy} = \frac{dU(y,t)}{dt} - \dot{q}_{amb}(y,t) \tag{5}$$

$$T_{HTF}(y=0,t) = T_{in}(t);\ \forall t > 0 \tag{6}$$

$$T(x,y,z,t=0) = T_{ini};\ \forall\, x,y,z\ \in V \tag{7}$$

Equation (5) forms the basis for the models developed for exclusively sensible [33] and latent [34, 35] storage systems. In these models, the internal energy $U(y_1, t_1)$ and heat loss $\dot{q}_{\mathrm{amb}}(y_1, t_1)$ at a specific height y_1 and time t_1 are written as a function of the local HTF temperature $T_{HTF}(y_1, t \in [0, t_1])$. An ordinary differential equation describing the HTF temperature is obtained by implementing the expressions for internal energy and heat loss into Equation (5). Resolving this ordinary differential equation results in an expression for both the heat loss and the outlet HTF temperature as a function of time and the size of the system (the y parameter).

Two important remarks can be made regarding this procedure. Firstly, the internal energy change is only a function of the local HTF temperature and time and not of the internal energy directly above or below the local position. This neglects heat conduction along the y-axis in the container wall and PCM. Furthermore, advection along the y-axis is present both in the HTF as in the storage material. The effect of neglecting heat conduction is quantified in [33] using two dimensional numbers: the cross conduction number and the thermocline width ratio. For the present case, the numbers indicate the heat conduction can be neglected if there is no or negligible natural convection in the PCM. However, previous studies showed that there is significant natural convection during melting [24], while it is usually negligible during solidification. This might result in a better model performance for solidification cases compared to melting cases.

The second remark concerns the limitations of the procedure to either sensible or latent heat. The integration cannot take the internal energy of the HTF, the sensible heat and the latent heat into account. In a LTES heat exchanger, these components are of course all present. As discussed in the introduction, a space-series-approach was suggested in [36] to combine the different sub-models. The space-series-approach integrates Equation (5) for each of the three sub-models separately. Subsequently it establishes a hierarchy between the sub-models: first the HTF model, secondly the sensible heat model and thirdly the latent heat model. The first model predicts the energy change based on the inlet condition of the LTES system, the second model based on the outlet of the first model and the third model based on the outlet of the second model (Equations (8), (9) and (10)). Equations (11), (12), (13), (14) and (15) define the energy modeled in each of the sub-heat exchangers.

$$\dot{m}_{HTF} c_{HTF} (T_{out} - T_{in}) = \left.\frac{dU_{HTF}}{dt}\right|_{\dot{m},T_{in}} + \left.\frac{dU_{sens}}{dt}\right|_{\dot{m},T_{HTF}^{out}} + \left.\frac{dU_{lat}}{dt}\right|_{\dot{m},T_{sens}^{out}} - \dot{Q}_{loss} \tag{8}$$

With

$$T_{HTF}^{out} = T_{in} + \frac{1}{\dot{m}_{HTF} c_{HTF}} \left.\frac{dU_{HTF}}{dt}\right|_{\dot{m}_{HTF},T_{in}} \tag{9}$$

$$T_{sens}^{out} = T_{HTF}^{out} + \frac{1}{\dot{m}_{HTF} c_{HTF}} \left.\frac{dU_{sens}}{dt}\right|_{\dot{m}_{HTF},T_{HTF}^{out}} \tag{10}$$

$$U_{HTF}(t) = \iiint \rho_{HTF} c_{HTF} T_{HTF}(x,y,z,t)\, dV_{HTF} \tag{11}$$

$$U_{sens}(t) = U_{CON}(t) + U_{PCM}^{sens}(t) \tag{12}$$

$$U_{CON}(t) = \iiint \rho_{CON} c_{CON} T_{CON}(x,y,z,t)\, dV_{CON} \tag{13}$$

$$U_{PCM}^{sens}(t) = \iiint \rho_{PCM} c_{PCM} T_{PCM}(x,y,z,t)\, dV_{PCM} \tag{14}$$

$$U_{lat}(t) = \iiint \rho_{PCM} h_{lat} \lambda(x,y,z,t)\, dV_{PCM} \tag{15}$$

The reason this approach is referred to as the space-series-method is that it is analogous to splitting the heat exchanger into three sub-heat exchangers (HTF, sensible heat and latent heat) and connecting them in series. The remaining question is defining the three sub-models and modelling the heat loss.

3.3. Sub-models

3.3.1. Heat transfer fluid sub-heat exchanger

The heat transfer fluid model is based on two extreme cases: a perfectly mixed vessel or a plug flow model. In a perfectly mixed vessel, the incoming fluid is mixed with the fluid in the heat exchanger. This model is described by the ordinary differential equation given below (Equation (16)). Equation (17) defines the average HTF temperature and Equation (18) defines the total HTF mass in the system.

$$\frac{dT_{HTF}}{dt} = \frac{\dot{m}_{HTF}}{m_{HTF}}(T_{in} - T_{HTF}) \tag{16}$$

$$T_{HTF}(t) = \frac{1}{V_{HTF}} \iiint T_{HTF}(x,y,z,t)\, dV_{HTF} \tag{17}$$

$$m_{HTF} = \rho_{HTF}\, D\, L\, w_{HTF} \tag{18}$$

In the case the inlet temperature is a step function with the step at time zero, the solution of this differential equation is given by Equation (19).

$$T_{HTF} = T_{in} + (T_{ini} - T_{in})\, e^{-t\frac{\dot{m}_{HTF}}{m_{HTF}}} \tag{19}$$

Equation (16) cannot be solved in general, however an elegant solution exists in the Laplace domain, as the mixed vessel is a first order system. Furthermore, an expression of the outlet temperature of the HTF sub-heat exchanger in the Laplace domain will be useful as input for the sensible heat exchanger. The expression in the Laplace domain is based on a dimensionless temperature θ defined by Equation (20).

$$\theta = \frac{T - T_{ini}}{T_{in} - T_{ini}} \tag{20}$$

The HTF outlet temperature in the Laplace domain $\tilde{\theta}_{HTF}$ is given by Equation (21).

$$\tilde{\theta}_{HTF}^{out} = \frac{\tilde{\theta}_{in}}{1 + m_{HTF}/\dot{m}_{HTF}\ p} \tag{21}$$

With
$\tilde{\theta}_{HTF}^{out}$ The Laplace transform of the HTF outlet temperature
$\tilde{\theta}_{in}$ The Laplace transform of the inlet temperature
p The Laplace transform parameter

The second extreme case for HTF modeling is plug bulk flow, where the incoming HTF and the HTF inside the heat exchanger do not mix. As a result, the outlet temperature of this system is given by the initial HTF temperature until the mass in the HTF channel is replaced. A plug bulk flow model is expressed by Equation (22) in the time domain and Equation (23) in the Laplace domain.

$$T_{HTF}^{out} = \begin{cases} T_{ini}, & t < m_{HTF}/\dot{m}_{HTF} \\ T_{in}(t - m_{HTF}/\dot{m}_{HTF}), & t \geq m_{HTF}/\dot{m}_{HTF} \end{cases} \tag{22}$$

$$\tilde{\theta}_{HTF}^{out} = \exp\left(-\frac{m_{HTF}}{\dot{m}_{HTF}}\ p\right)\tilde{\theta}_{in} \tag{23}$$

The plug bulk flow and mixed vessel models can be combined by introducing a parameter $r_{HTF,}$ which denotes the amount of mass that behaves as a perfectly mixed vessel. The outlet temperature in the Laplace domain is given by Equation (24).

$$\tilde{\theta}_{HTF}^{out} = \exp\left(-r_{HTF}\frac{m_{HTF}}{\dot{m}_{HTF}}\,p\right)\frac{\tilde{\theta}_{in}}{1+(1-r_{HTF})\frac{m_{HTF}}{\dot{m}_{HTF}}\,p} \tag{24}$$

3.3.2. Sensible sub-heat exchanger

3.3.2.1. Local heat transfer model

The first step in developing the sensible sub-heat heat exchanger model is a relation between the local HTF temperature and the heat flux to the container and storage material, i.e. the local heat transfer model. Furthermore, the heat loss has to be linked to the HTF and ambient temperature. These relations are developed using thermal quadrupoles as described by Maillet et al. [44]. Such a thermal quadrupole links temperature and heat flux on one side of the body to the temperature and heat flux at the other side of the body for unidirectional heat flux and material properties, which are not temperature-dependent. The dimensionless temperature is defined as Equation (20), while the heat flux is defined referenced to the temperature difference $T_{in} - T_{ini}$.

$$\varphi = \frac{\dot{Q}}{A\,(T_{in} - T_{ini})} \tag{25}$$

The thermal quadrupole links the Laplace transform of the dimensionless temperature $\tilde{\theta}_L$ and heat flux $\tilde{\varphi}_L$ on the left-hand side of the body to the dimensionless temperature $\tilde{\theta}_R$ and heat flux $\tilde{\varphi}_R$ on the right-hand side of the body (Equation (26)). The quadrupole functions (m_{ii}) depend on the geometry of the body (see [44]).

$$\begin{bmatrix}\tilde{\theta}_L\\ \tilde{\varphi}_L\end{bmatrix} = \begin{bmatrix}m_{11} & m_{12}\\ m_{21} & m_{22}\end{bmatrix}\begin{bmatrix}\tilde{\theta}_R\\ \tilde{\varphi}_R\end{bmatrix} \tag{26}$$

With

$\tilde{\theta}_L$	The Laplace transform of the dimensionless temperature on the left-hand side of the plate.
$\tilde{\varphi}_L$	The Laplace transform of the heat flux on the left-hand side of the plate.
$\tilde{\theta}_R$	The Laplace transform of the dimensionless temperature on the right-hand side of the plate.
$\tilde{\varphi}_R$	The Laplace transform of the heat flux on the right-hand side of the plate.
m_{ii}	Thermal quadrupole functions.

For heat conduction in a flat-plate, the quadrupole functions are given by Equations (27), (28), (29) and (30) [44].

$$m_{11}(p) = cosh\left(\sqrt{\frac{p}{\alpha}}\,w\right) \tag{27}$$

$$m_{12}(p) = \frac{sinh\left(\sqrt{\frac{p}{\alpha}}\,w\right)}{k\sqrt{\frac{p}{\alpha}}} \tag{28}$$

$$m_{21}(p) = \sqrt{\frac{p}{\alpha}}\,k\,sinh\left(\sqrt{\frac{p}{\alpha}}\,w\right) \tag{29}$$

$$m_{22}(p) = cosh\left(\sqrt{\frac{p}{\alpha}}\, w\right) \tag{30}$$

With α The thermal diffusivity of the material
k The thermal conductivity of the material
w The width of the material

Convective boundary conditions link the conditions at the left-hand side of the storage materials and on the right-hand side of the PCM with respectively the HTF temperature and the ambient temperature. These boundary conditions can be expressed as a thermal quadrupole as Equation (31) and (32) (see [44]).

$$\begin{bmatrix} \tilde{\theta}_{HTF} \\ \tilde{\varphi}_{HTF} \end{bmatrix} = \begin{bmatrix} 1 & 1/\mathrm{h} \\ 0 & 1 \end{bmatrix} \begin{bmatrix} \tilde{\theta}_L^{CON} \\ \tilde{\varphi}_L^{CON} \end{bmatrix} \tag{31}$$

With $\tilde{\varphi}_{HTF}$ The Laplace transform of the heat flux from the HTF
h Convective heat transfer coefficient.

$$\begin{bmatrix} \tilde{\theta}_R^{PCM} \\ \tilde{\varphi}_R^{PCM} \end{bmatrix} = \begin{bmatrix} 1 & 1/U_{loss} \\ 0 & 1 \end{bmatrix} \begin{bmatrix} \tilde{\theta}_{amb} \\ \tilde{\varphi}_{amb} \end{bmatrix} \tag{32}$$

$\tilde{\theta}_{amb}$ The Laplace transform of the dimensionless temperature of the ambient.
$\tilde{\varphi}_{amb}$ The Laplace transform of the heat flux to the ambient
U_{loss} Overall heat transfer coefficient from the PCM to the ambient

Figure 7 shows the local heat transfer section of the flat-plate heat exchanger translated to the thermal quadrupole. On the left-hand side is the HTF temperature $\tilde{\theta}_{HTF}$, which is linked to the left-hand side of the container $\begin{bmatrix} \tilde{\theta}_L^{CON} \\ \tilde{\varphi}_L^{CON} \end{bmatrix}$ through a convective heat transfer coefficient *h* (the quadrupole matrix defined in Equation (31)). The behavior of the container material and PCM material is modeled by two flat-plate quadrupoles with respectively the container and PCM material properties. Finally, the heat transfer to the ambient is modeled as the quadrupole defined as Equation (32).

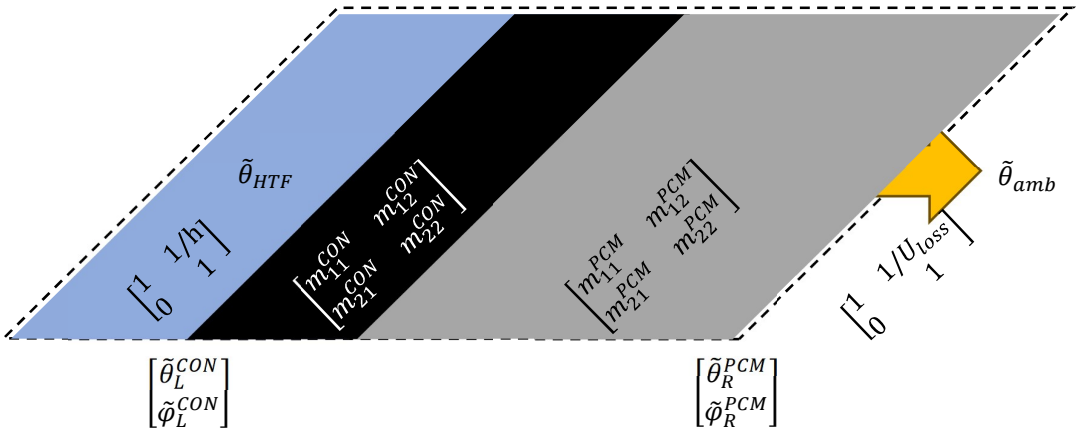

Figure 7: Thermal quadrupoles applied to local heat transfer under the parallel plate assumption.

Combining the quadrupoles shown in Figure 7 results in a relationship between the temperature and heat flux of the HTF and the ambient.

$$\begin{bmatrix} \tilde{\theta}_{HTF} \\ \tilde{\varphi}_{HTF} \end{bmatrix} = \begin{bmatrix} M_{11} & M_{12} \\ M_{21} & M_{22} \end{bmatrix} \begin{bmatrix} \tilde{\theta}_{\mathrm{amb}} \\ \tilde{\varphi}_{\mathrm{amb}} \end{bmatrix} \tag{33}$$

$$M_{11} = \frac{1}{h}\left(m_{21}^{PCM}\left(m_{12}^{CON}\,h + m_{22}^{CON}\right) + m_{11}^{PCM}\left(m_{11}^{CON}\,h + m_{21}^{CON}\right)\right) \tag{34}$$

$$M_{12} = \frac{1}{hU}\left(m_{21}^{PCM}\left(m_{12}^{CON}\,h + m_{22}^{CON}\right) + m_{11}^{PCM}\left(m_{11}^{CON}\,h + m_{21}^{CON}\right) + U\left(m_{12}^{PCM}\left(m_{11}^{CON}\,h + m_{21}^{CON}\right) + m_{12}^{CON}h^2 + m_{22}^{CON}h\right)\right) \tag{35}$$

$$M_{12} = m_{22}^{CON}m_{21}^{PCM} + m_{21}^{CON}m_{11}^{PCM} \tag{36}$$

$$M_{22} = \frac{1}{U}\left(m_{22}^{CON}m_{21}^{PCM} + m_{21}^{CON}m_{11}^{PCM} + U\,m_{21}^{CON}\,m_{12}^{PCM} + m_{22}^{CON}\,h\,U\right) \tag{37}$$

Equation (33) can be used to link the HTF and ambient temperature ($\tilde{\theta}_{HTF}$ and $\tilde{\theta}_{\mathrm{amb}}$) to the heat flux to the storage material ($\tilde{\varphi}_{HTF}$ Equation (38)) and the heat loss ($\tilde{\varphi}_{\mathrm{amb}}$ Equation (39)).

$$\tilde{\varphi}_{HTF} = \frac{M_{22}}{M_{12}}\tilde{\theta}_{\mathrm{HTF}} + \left(M_{21} - \frac{M_{22}M_{11}}{M_{12}}\right)\tilde{\theta}_{\mathrm{amb}} \tag{38}$$

$$\tilde{\varphi}_{amb} = \frac{1}{M_{12}}\tilde{\theta}_{\mathrm{HTF}} - \frac{M_{11}}{M_{12}}\tilde{\theta}_{\mathrm{amb}} \tag{39}$$

Equations (38) and (39) constitute the local heat transfer model for the storage system, which determines the heat fluxes as a function of the known temperatures. The ambient temperature can be assumed to be known, as it is independent of the operation of the storage system. On the contrary, the local bulk HTF temperature is only known at the inlet of the system. In the rest of the heat exchanger, it depends on the upstream heat transfer to the storage material. The next subsection uses the local heat transfer model to obtain the sensible sub-heat exchanger model.

3.3.2.2. Heat transfer fluid integration

The relation between the HTF temperature and the local heat transfer section was defined in Equation (5) as an ordinary differential equation defining the behavior along the z-axis. In terms of the thermal quadrupoles developed above, the equation can be rewritten as Equation (40). There are three major differences between Equation (5) and Equation (40). Firstly, the equation is expressed in the Laplace domain. This transformation is allowed if the spatial and temporal variable are independent [45]. Secondly, the spatial variable is no longer the position along the z-axis but rather the heat transfer surface area A. This makes the solutions in this section more general, as they will also apply to non-planar geometries if the quadrupole coefficients are adapted accordingly. Thirdly, the right-hand side of the equation is the heat flux from the HTF to the container, as there is an expression for this value defined by Equation (38).

$$\dot{m}_{HTF}c_{HTF}\frac{d\tilde{\theta}_{HTF}}{dA} = -\tilde{\varphi}_{HTF} \tag{40}$$

With at the inlet (A=0): $\tilde{\theta}_{HTF}(A = 0) = \tilde{\theta}_{in}$
With as initial condition (t=0): $\theta_{ini} = 0$

With A Surface area

$\dot{m}$ Mass flow rate of the HTF

c_{HTF} Specific heat capacity

By substituting Equation (38) into the differential equation above, the equation below is obtained as Equation (41).

$$\dot{m}_{HTF} c_{HTF} \frac{d\tilde{\theta}_{HTF}}{dA} = -\frac{M_{22}}{M_{12}} \tilde{\theta}_{\mathrm{HTF}} - \left(M_{21} - \frac{M_{22} M_{11}}{M_{12}} \right) \tilde{\theta}_{\mathrm{amb}} \tag{41}$$

The above equation can be solved to obtain the behavior of the temperature $\tilde{\theta}_{HTF}$ as a function of the position in the heat exchanger *A*.

$$\begin{aligned} \tilde{\theta}_{HTF}(A,p) = \tilde{\theta}_{HTF}(A=0) \exp\left(-\frac{M_{22}}{M_{12}} \frac{A}{\dot{m}_{HTF} c_{HTF}} \right) + \\ \tilde{\theta}_{\mathrm{amb}} \left(\frac{M_{21} M_{12} - M_{22} M_{11}}{M_{22}} \right) \left(\exp\left(-\frac{M_{22}}{M_{12}} \frac{A}{\dot{m}_{HTF} c_{HTF}} \right) - 1 \right) \end{aligned} \tag{42}$$

The total heat transferred from the HTF and the losses to the ambient can be determined by substituting Equation (42) in respectively Equation (38) and Equation (39) and integrating over the surface area A. The difference between the total heat transferred from the HTF and the losses to the ambient is the stored energy in the sensible sub heat exchanger.

The solution developed up to this point are described in the Laplace domain. There is no analytical expression for these solutions in the time domain. Therefore, numerical inversion is used as described in [45].

3.3.3. Latent sub-heat exchanger

The latent sub-heat exchanger model is described in [34, 35]. The present section gives a brief overview of the model in order to explain the major assumptions and simplifications.

The latent sub-heat exchanger only considers the latent heat of phase change. Therefore, the internal energy of the latent sub heat exchanger can be expressed as a function of the liquid fraction: the ratio of liquid to total PCM. With constant PCM density assumed, the liquid fraction is a geometrical parameter; it follows from the position of the phase change front in the heat exchanger. In the context of the local heat transfer model, the local liquid fraction is defined as Equation (43) with the local internal latent energy $U_{lat}(y,t)$ defined by Equation (44).

$$\lambda(y,t) = \int_0^D \int_{w_{HTF}+w_{CON}}^{w_{HTF}+w_{CON}+w_{PCM}} \lambda(x,y,z,t) dx\, dz \tag{43}$$

$$U_{lat}(y,t) = \rho_{PCM} h_{lat} h_{lat}(y,t) \tag{44}$$

Since only latent heat is considered in the present sub-model, all heat from the HTF is transferred to the phase change front: the interface between solid and liquid PCM. This phase change front is always at the phase change temperature since isothermal phase change is assumed in the present model. The driving temperature difference for heat transfer is thus given by the difference between the local HTF temperature and the phase change temperature. The thermal resistance from the HTF to the phase change front also changes with the liquid fraction. This thermal resistance is the sum of the convective resistance in the HTF, the conductive resistance of the wall and the resistance between the container and the phase change front. In the case of solidification, this latter resistance is conductive, while in the case of melting, this resistance is a combination of initial conduction and later natural convection. In conductive heat transfer, the heat transfer resistance is a function of the phase change front position and thus of the liquid fraction, while in convective heat transfer the heat transfer rate depends on the

driving temperature range and thus of the local HTF temperature. This dependency on the temperature is neglected. As a result, the heat transfer resistance is a function of the liquid fraction $R(\lambda)$, not the local HTF temperature both for solidification and for melting.

A local energy balance for the latent heat can be written as Equation (45). The local internal energy described on the left-hand side of the equation is solely a function of the local liquid fraction. The heat transfer rate to the phase change front is a function of the phase change temperature T_{pc}, the local HTF temperature T_{HTF} and the local heat transfer resistance $R(\lambda(y,t))$.

$$\rho_{PCM} h_{lat} \frac{d\lambda(y,t)}{dt} = \frac{1}{R(\lambda(y,t))}(T_{pc} - T_{HTF}) \tag{45}$$

With T_{pc} The phase change temperature

T_{HTF} The local THF temperature

Equation (45) can be resolved by separating the variables, which results in a function which describes the local liquid fraction. This local liquid fraction is a function of time and the time-averaged temperature difference between the HTF and phase change front $\Delta\overline{\mathrm{T}}$ defined by Equation (46). Note that the averaging operator in the latent heat model serves a similar role as the Laplace transform in the sensible heat model: the effect of the time dependence of the driving temperature difference is captured by an integral transformation, which allows for use of a local model for any variation in this driving temperature difference.

$$\Delta\overline{\mathrm{T}} = \frac{1}{t}\int_0^t (T_{pc} - T_{HTF})\mathrm{dt} \tag{46}$$

Local solidification heat transfer model

The local solidification heat transfer model is based on conductive heat transfer from the container wall to the phase change front. As derived in [35], the local liquid fraction is given by Equation (47).

$$\lambda_{loc}(t, \Delta\overline{\mathrm{T}}) = \frac{1}{w_{PCM}}\left[\frac{-k_{PCM}}{h} + \sqrt{\left(\frac{k_{PCM}}{h}\right)^2 + \frac{2\,k_{PCM} t \Delta\overline{\mathrm{T}}}{h_{lat}\rho_{PCM}}}\right] \tag{47}$$

The liquid fraction defined by Equation (47) for the present case is shown on Figure 8.

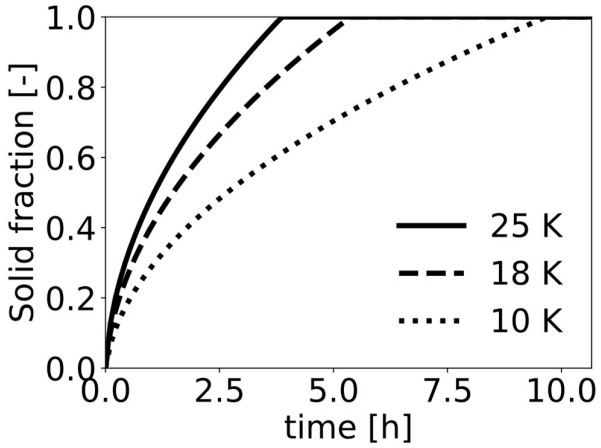

Figure 8: Liquid fraction as a function of time for the solidification sub-model.

In order to integrate the local liquid fraction to obtain the overall liquid fraction, the local liquid fraction is written as the product of a function of time and a power law for the effect of the average temperature difference (Equation (48)).

$$\lambda_{loc}(t, \Delta\overline{\mathrm{T}}) \approx f(t)\, \Delta\overline{\mathrm{T}}^{r(t)} \tag{48}$$

The effect of this approximation is studied in [46]. For planar geometries, the resulting error is small.

Local melting heat transfer model

The PCM melting is dominated by natural convection. In a prior CFD study on melting of this PCM [41], a correlation is proposed for a natural convection enhancement rate, which is defined as the ratio of the melting time to the phase change time if there is no natural convection Equation (49).

$$Enhancement\ Rate(\Delta T_{inlet}) = \begin{cases} 1 \quad if\ {Ra_W}^{1/6}\left(\frac{L}{w_{PCM}}\right)^{-\frac{1}{4}} < 2.73 \\ 0.57\ {Ra_W}^{1/6}\left(\frac{L}{w_{PCM}}\right)^{-\frac{1}{4}} - 0.38 \quad if\ {Ra_W}^{1/6}\left(\frac{L}{w_{PCM}}\right)^{-\frac{1}{4}} \geq 2.73 \end{cases} \tag{49}$$

$$Ra_W = \frac{g\ \beta\ \Delta T\ {w_{PCM}}^3}{\upsilon\alpha} \tag{50}$$

With g Gravitational acceleration [m/s²]

β Coefficient of thermal expansion [1/K]

ΔT Temperature difference between the container wall and phase change temperature [K]

υ Kinematic diffusivity of the PCM [m²/s]

α Thermal diffusivity of the PCM [m²/s]

Melting in a rectangular enclosure undergoes four phases: conduction, early convection, steady convection and shrinking solid [47]. All four phases have different heat transfer behavior [48]. In order to simplify the current model, the steady convection stage is assumed to be dominant. The local liquid fraction is thus defined as Equation (51) with t_{con} the time for complete phase change if no natural convection is present [2].

$$\lambda_{loc}(t, \Delta\overline{\mathrm{T}}) = Enhancement\ Rate(\Delta T_{inlet})\ \frac{t}{t_{con}} \frac{\Delta\overline{\mathrm{T}}}{\Delta \mathrm{T}_{inlet}} \tag{51}$$

$$t_{con} = \frac{h_{lat} \rho_{PCM} {w_{PCM}}^2}{2\ k_{PCM} \Delta \mathrm{T}_{inlet}} \left(1 + 2\frac{k_{PCM}}{h\ w_{PCM}}\right)^2 \tag{52}$$

The resulting liquid fraction as a function of time for the three driving temperature differences is shown in Figure 9.

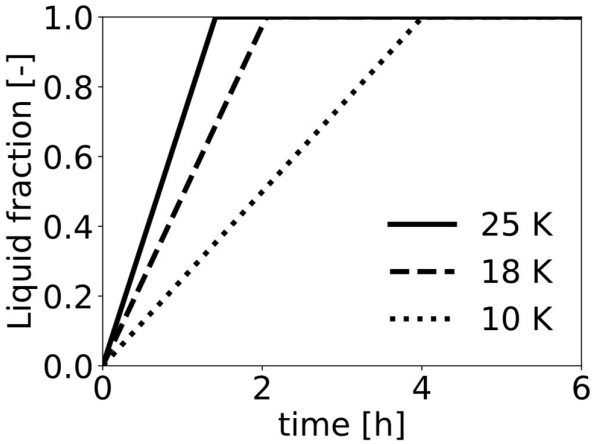

Figure 9: Liquid fraction as a function of time for the melting sub-model.

The local liquid fraction functions are used to determine the local HTF temperature via a similar technique as used for the sensible heat exchangers. This method was already discussed in prior work and will not be repeated here [34, 35].

4. Result and discussion

This section discusses the experimental results and the performance of the predictive model. The discussion of the model is split into a description of the experimental results and the energy balance, a description of the method used to obtain a Laplace transform for the inlet temperature and a discussion of the predictions of the model for the solidification and melting cases.

This section compares the measured and predicted HTF temperature at both the inlet and the outlet. Therefore, it is useful to adopt metrics to quantify the difference between two discrete time series. Two metrics are chosen: the maximal deviation and the average deviation.

4.1. Experimental results and energy balance

The experimental matrix contains twelve types of experiments: six solidification experiments and six melting experiments. These six experiments are the result of a full factorial design with two levels of HTF volume flow rate (2 m³/h and 0.5 m³/h) and three temperature levels (25 K, 18 K and 10 K) where the temperature level is defined as the temperature difference between the HTF temperature setpoint and the phase change temperature. The main measurements of concern here are the inlet and outlet temperature of the HTF.

Figure 10 shows the inlet and outlet temperature for all melting experiments. The experiments are organized according to the driving temperature difference (horizontal) and the volumetric flow rate (vertical). Multiple experiments were performed for each setpoint in the experimental matrix, with a total of 24 cases. Each graph also features an error bar which indicates the measurement error on the temperature difference on the scale of the graph.

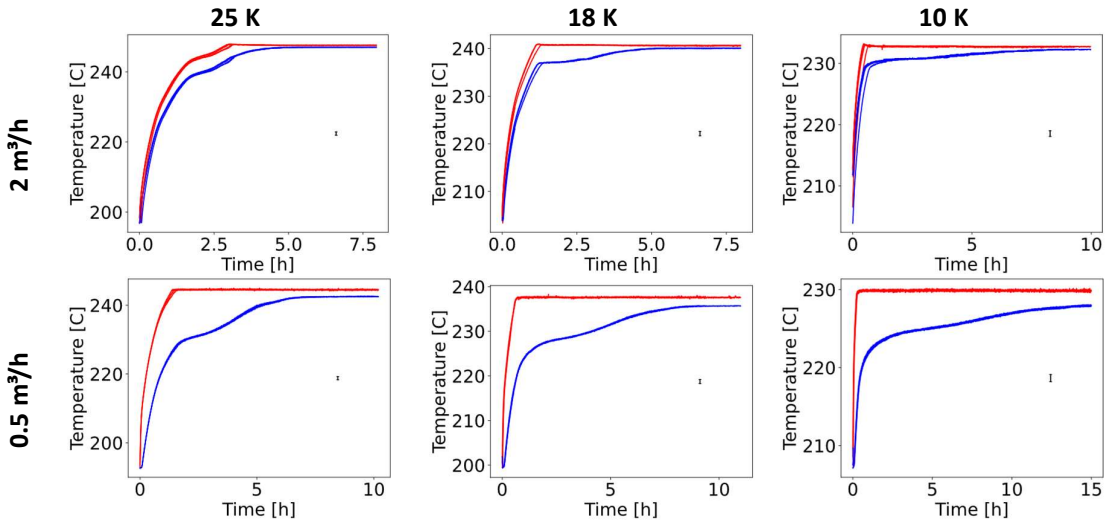

Figure 10: HTF inlet (red) and outlet (blue) temperature for the 6 experiment types for the melting experiments. All 24 performed experiments are shown. The error bars show the error of the sensors on the temperature difference between the inlet and outlet temperature.

Figure 11 is the equivalent to Figure 10 for the solidification cases. A total of 20 solidification experiments are included.

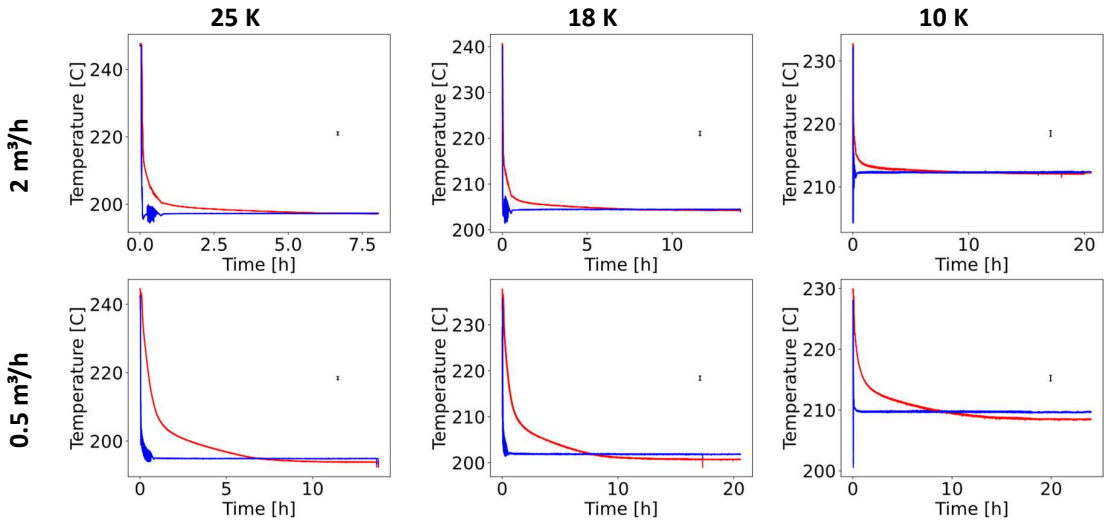

Figure 11: HTF inlet (red) and outlet (blue) temperature for the 6 experiment types for the solidification experiments. The error bars show the error of the sensors on the temperature difference between the inlet and outlet temperature.

The heat losses can be estimated by performing an energy balance on the system. The energy balance compares the total energy transferred from or to the HTF (i.e. the total efflux of energy defined by Equation (53)) with the energy change of HTF, container and PCM mass from the initial to the inlet temperature (i.e. the stored energy defined by Equation (54)). The temperature difference between the initial and final state of the system has to be estimated as it is not measured in a high enough spatial resolution to capture the non-uniform nature of the temperature field. Therefore, the initial and final temperatures are estimated as the bulk HTF temperature at the start and end of the experiment (Equation (58) and (59)).

$$\Delta E = \int_0^t \dot{V}_{HTF}(t)\rho_{HTF}c_{HTF}\big(T_{out}(t) - T_{in}(t)\big)\,dt \tag{53}$$

$$\Delta U = (V_{HTF}\rho_{HTF}c_{HTF} + M_{CON}c_{CON})\Delta T_{tot} + M_{PCM}(h_{lat} + c_{PCM}^{liq}\Delta T_{liq} + c_{PCM}^{sol}\Delta T_{sol}) \tag{54}$$

$$\Delta T_{tot} = |T_{ini} - T_{end}| \tag{55}$$

$$\Delta T_{liq} = \begin{cases} T_{ini} - T_{pc} \; if \; solidification \\ T_{pc} - T_{end} \qquad if \; melting \end{cases} \tag{56}$$

$$\Delta T_{sol} = \begin{cases} T_{pc} - T_{end} \; if \; solidification \\ T_{pc} - T_{ini} \qquad if \; melting \end{cases} \tag{57}$$

$$T_{ini} = \frac{1}{2}\big(T_{out}(t=0) + T_{in}(t=0)\big) \tag{58}$$

$$T_{end} = \frac{1}{2}\big(T_{out}(t_{end}) + T_{in}(t_{end})\big) \tag{59}$$

The efflux of energy and stored energy are compared in Figure 12 where the error bars are determined as described in Appendix A. In terms of the stored energy on the horizontal axis, the data falls in three groups according to the inlet temperature setpoint. A larger temperature difference setpoint leads to a higher amount of stored energy. In terms of the deviation between the efflux of energy and the stored energy, the data can be split into two groups: solidification and melting. For the melting experiments above the black lines, more efflux is required compared to the stored energy as the HTF has to compensate for the heat loss. In contrast, the solidification experiments have a lower efflux of energy than the total stored energy due to the losses contributing to the decrease in internal energy of the system. A final trend that can be distinguished is the effect of the volume flow rate of the experiment. For the melting experiments, a lower volumetric flow rate results in a longer experiment time and thus more total heat losses.

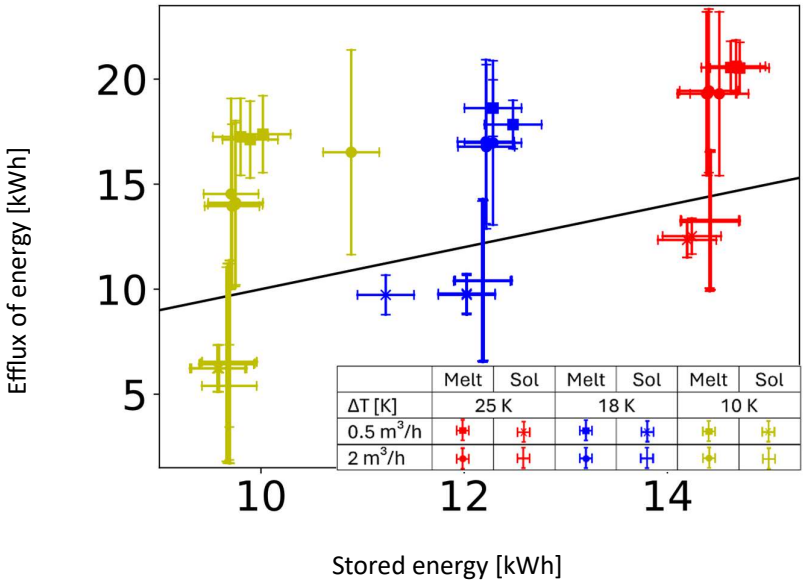

Figure 12: Comparison of the total efflux of energy with the total stored energy. The black line indicates equality between both values.

The heat losses can also be quantified by defining an overall heat loss coefficient. As can be seen from the temperature data presented in Figure 10 and Figure 11, the end of the experiment for all but the longest experiments feature a period with a stable temperature difference between inlet and outlet temperature. The system seems to have reached a steady state, where the efflux of energy of the HTF is transferred to the environment. The ratio of the efflux at the end of the experiment to the

temperature difference between the ambient and the system can be used as an estimate of the overall heat loss coefficient (Equation (60).

$$UA_{loss}^{end} = \frac{\dot{m}c_p\left(T_{in}(t_{end}) - T_{out}(t_{end})\right)}{T_{end} - T_{amb}} \tag{60}$$

An alternative calculation of the overall heat loss coefficient can be based on the difference between the total efflux of energy and the stored energy shown in Figure 12. The total losses can be estimated based on the difference between total efflux of energy and the stored energy. The overall heat loss coefficient is assumed constant and not a function of the state of the system. Furthermore, the average temperature of the system is assumed constant as well as the average of the initial and final temperature. With these assumptions, the overall heat loss coefficient is equal to the total losses divided by the average temperature difference between the system and the ambient and the total time of the experiment (Equation (61)).

$$UA_{loss}^{avg} = \frac{|\Delta E - \Delta U|}{t_{end}\left(\frac{1}{2}\left(T_{ini} + T_{end}\right) - T_{amb}\right)} \tag{61}$$

Both calculation methods are compared in Figure 13. The error bars are determined as described in Appendix A, however only the error bars for the cases with a volume flow rate of 0.5 m³/h are shown. The error is dominated by the measurement error on the temperature difference between the inlet and outlet of the heat transfer fluid. This temperature difference is smaller for the cases with a volume flow rate of 2 m³/h and therefore the error is comparatively larger than for the cases with 0.5 m³/h. The error for the 2 m³/h are too large to draw significant conclusions and therefore the conclusions are based on the 0.5 m³/h cases. The 2 m³/h cases are added as a reference. .

The overall heat loss coefficients for both calculation methods agree remarkably well as most points deviate within the error bars. The estimated coefficients form two groups: one between 0.6 and 1.6 W/K for the solidification experiments and one between 2.4 and 2.6 W/K for the melting experiments.

The error on the y-axis is the result of the difference between initial and final temperature, which is larger for larger driving temperature differences. The error on the x-axis due to the temperature measurement uncertainty is much larger. This error strongly depends on the volumetric flow rate of the HTF: a lower flow rate means a larger temperature difference between inlet and outlet and, as a result, a lower relative impact of the measurement uncertainty.

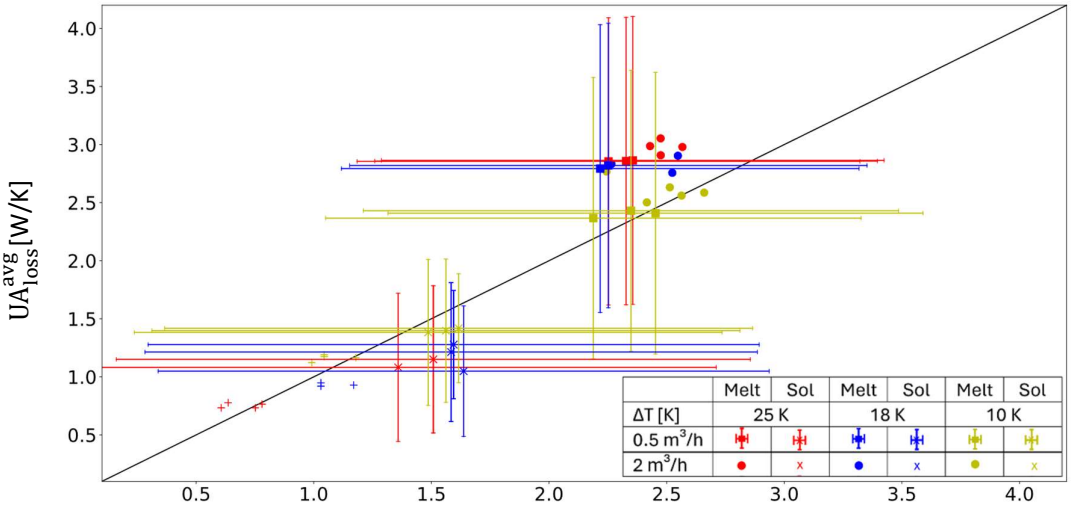

UA_{loss}^{end} [W/K]

Figure 13: Comparison of the total efflux of energy with the total stored energy. The black line indicates equality between both values.

The heat loss coefficient can also be estimated based on the geometry of the system. Based on the parallel plate assumption, the total thermal resistance from the HTF to the ambient can be estimated as about 0.54 W/K at the minimal experimental temperature and 0.64 W/K at the higher end of the temperature range. Insulation material results in 97% of this thermal resistance. The difference between the upper and lower limit is due to the temperature dependency of the insulation material.

The heat loss coefficient determined based on the geometry and insulation material properties underestimate the measured heat loss coefficient by a factor of maximum four. One possible explanation for this discrepancy is losses through the inlet and outlet tubing. Since these losses are hard to evaluate, the experimentally determined heat loss coefficient will be used to predict the output of the system with a value of for 1.25 W/K solidification and 2.5 W/K for melting.

4.2. Inlet temperature Laplace transform

The HTF and sensible sub-heat exchanger are expressed in the Laplace domain. Therefore, the inlet temperature needs to be transformed to the Laplace domain as well. This representation in the Laplace domain is preferably continuous. One method of obtaining such a continuous representation in the Laplace domain is approximating the inlet temperature signal as the sum of a base of functions with known Laplace transforms. The accuracy of the approximation depends on the choice of the base functions as well as the number of terms in the sum.

An obvious and complete basis for decomposition of a periodic function is a Fourier series, which can be interpreted as a sum of goniometric functions with known Laplace transforms. However, the inlet temperature features a step change at the start of the experiment, which requires a large amount of terms in the Fourier series to approximate accurately. Therefore, the step change is first fitted with a first order system responding to a step change. The residual difference between the measured inlet temperature and the first order system is subsequently fitted by a Fourier series. Following this procedure, the dimensionless inlet temperature is approximated by Equation (62) in the time domain and Equation (63) in the Laplace domain.

$$\theta_{in}(t) \approx \left(1 - exp\left(-\frac{t}{\tau_{FO}}\right)\right) + \frac{a_0}{2} + \sum_{i=1}^{n_{Fourier}} \left[a_i \, cos\left(\frac{2\,\pi\,i}{t_{end}} t\right) + b_i \, sin\left(\frac{2\,\pi\,i}{t_{end}} t\right)\right] \tag{62}$$

$$\tilde{\theta}_{in}(p) \approx \frac{1}{p} - \frac{\tau_{FO}}{1 + \tau_{FO}\,p} + \frac{a_0}{2\,p} + \sum_{i=1}^{n_{Fourier}} \left[\frac{a_i\,p}{p^2 + \left(\frac{2\,\pi\,i}{t_{end}}\right)^2} + \frac{b_i\,\left(\frac{2\,\pi\,i}{t_{end}}\right)}{p^2 + \left(\frac{2\,\pi\,i}{t_{end}}\right)^2}\right] \tag{63}$$

With
- τ_{FO} Time constant of the first order system [s]
- a_0 First Fourier series term [-]
- a_i i^{th} Fourier series expansion coefficient cosine [-]
- b_i i^{th} Fourier series expansion coefficient sine [-]
- t_{end} Total time of the experiment
- $n_{Fourier}$ Number of Fourier terms in the approximation

The number of terms in the Fourier series is a compromise between accuracy of the approximation and the calculation time. The maximal and average deviation between measured and approximated temperature are used to assess the required number of terms in the Fourier series expansion for both the melting and solidification experiments.

For the solidification experiments, Table 6 reports the average and maximum deviation between measured and approximated inlet temperature for 40 terms in the Fourier series expansion. The average deviation is below 0.3 K for all cases which is low compared to the signal noise and sensor accuracy. The maximal deviation on the other hand is quite significant especially at the lower HTF volumetric flow rate. This maximal error occurs during the initial 300 seconds of the experiments, when the inlet temperature exhibits high frequency oscillations. In order to fit these high frequency variations, a very large number of terms would be required. Since the average error is low, the approximation with 40 terms is deemed sufficient.

Table 6: Maximal and average absolute difference between the measured inlet temperature and the approximation using 40 terms in the Fourier series for the solidification experiments.

		25 K		**18 K**		**10 K**	
2 m³/h	Max	6 K	Max	4.2 K	Max	7.9 K
	Average	0.14 K	Average	0.10 K	Average	0.05 K
0.5 m³/h	Max	12.5 K	Max	9.8 K	Max	9.8 K
	Average	0.22 K	Average	0.1 K	Average	0.08 K

Table 7 shows the maximal and average deviation between measured and approximated inlet temperature using 40 terms in the Fourier series for the melting experiments. The average deviation are below 0.2 K, which is acceptable. The maximal deviation is smaller than for the solidification cases. Similar to these cases, the maximal error occurs during the initial transient of the experiment.

Table 7: Maximal and average absolute difference between the measured inlet temperature and the approximation using 40 terms in the Fourier series for the melting experiments.

		25 K		**18 K**		**10 K**	
2 m³/h	Max	1.8 K	Max	1.8 K	Max	1.3 K
	Average	0.07 K	Average	0.06 K	Average	0.05 K
0.5 m³/h	Max	4.9 K	Max	3.7 K	Max	1.4 K
	Average	0.17 K	Average	0.11 K	Average	0.09 K

4.3. Solidification

The main goal of the heat exchanger model is to correctly predict the outlet temperature of the HTF as a function of the experimentally measured inlet temperature. However, the outlet temperature of the sub-heat exchangers can help to understand how the model functions. Therefore, the outlet temperature of each sub-heat exchanger is shown and discussed first. In order not to overextend the paper, this discussion is done for a single experiment, namely the experiment with a volumetric flow rate of 0.5 m³/h and a temperature difference of 25 K. The results for this experim ent are shown in Figure 14.

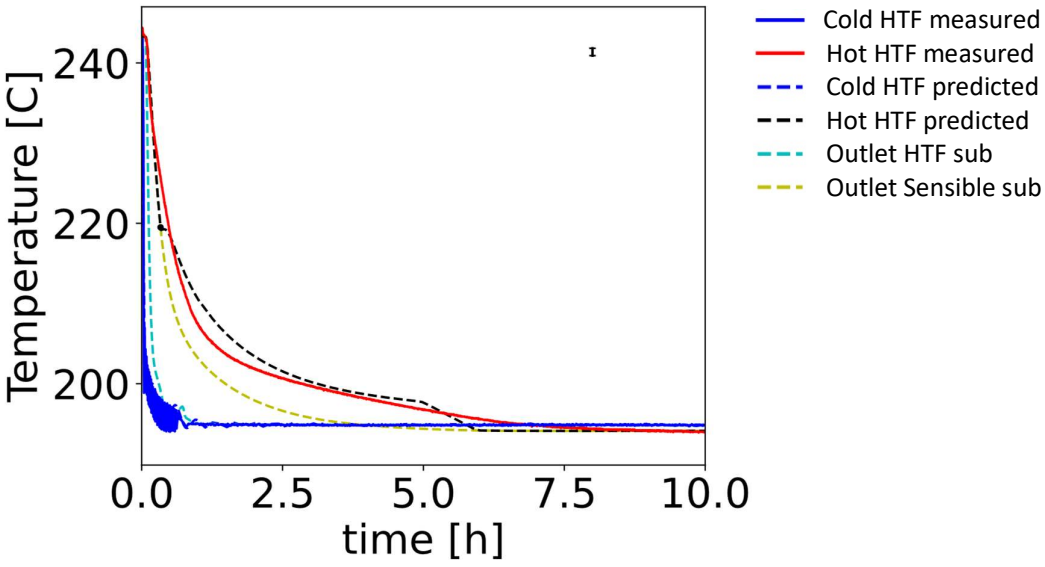

(a) Complete solidification experiment

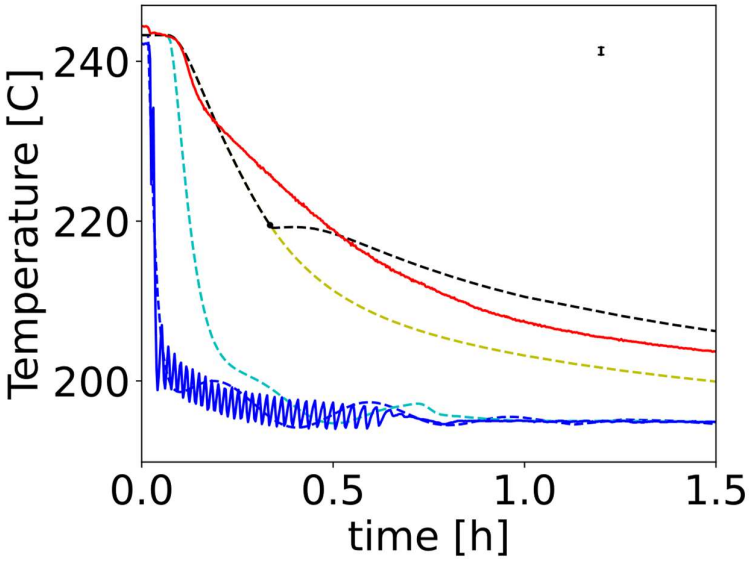

(b) Close-up of the first hour and a halve of a solidification experiment

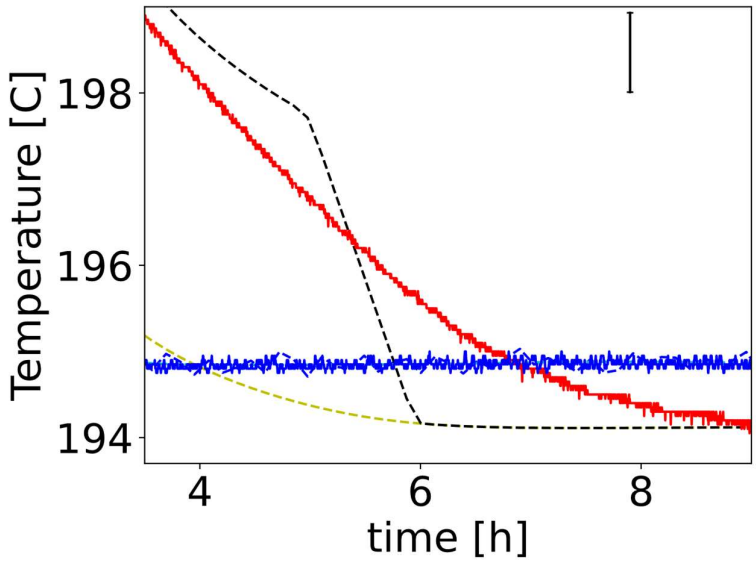

(c) Close-up of the predicted outlet temperature drop between 3 h and 9 h

Figure 14: Comparison of measured HTF temperatures with the predicted HTF temperatures with additional results for each of the sub-heat exchangers for the solidification case with a volumetric flow rate of 0.5 m³/h and a temperature difference of 25 K.

The outlet temperature prediction agrees quite well with the measured outlet temperature with a maximal deviation of 6.4 K and an average deviation of 0.8 K. The largest deviations can be found at the start of the experiment and around 5 h as shown close up in (b) and (c) of Figure 14.

The start of the experiment features both the sharpest variation in the inlet temperature (0 to 0.1 h) as well as the highest frequency variations with a significant amplitude (0.25 h to 50 h). As can be seen in on Figure 14 (b), the fitted inlet temperature does not include these high frequency oscillations and therefore the instantaneous energy transfer in this interval can deviate from the experimentally measured value. Nevertheless, the model predictions are satisfactory in this region.

The start of the experiment shown in Figure 14 (b) also shows the functioning of the three sub-heat exchanger models. The HTF sub-heat exchanger causes a delay between the change in inlet temperature and the heat transfer to the container and storage material. Its influence is dominant in the very early stages of charging, after which it becomes negligible compared to the sensible and latent heat transferred. This corresponds to the magnitude of mass conservation as the driving transfer mechanism for the HTF energy compared the magnitude of heat transfer for the sensible and latent heat sub-heat exchangers.

Once the outlet temperature of the HTF sub-heat exchanger drops below the initial temperature, the sensible sub-heat exchanger transfers heat to the HTF. Before the outlet temperature of the sensible sub-heat exchanger drops below the phase change temperature (demarcated by a black circle), the latent heat exchanger does not have any effect. As a result, the sensible heat is the dominant energy transfer in the system for a brief instant between the HTF sub-heat exchanger outlet temperature drop and the outlet temperature of the latent heat exchanger reaching the phase change temperature. In contrast to the HTF sub-heat exchanger, the sensible heat sub-heat exchanger remains relevant until the end of the experiment, partially due to its larger thermal mass compared to the HTF sub-heat exchanger, partially due to the effect of the heat losses that are included in this sub-heat exchanger.

Unlike the HTF and sensible sub-heat exchanger, the latent heat sub-heat exchanger can be completely inactive while the HTF and sensible sub-heat exchanger only asymptotically approach a steady state. The latent sub-heat exchanger, however, can be inactive because no latent heat is transferred before the inlet temperature drops below the phase change temperature (demarcated by the black circle) and secondly because the PCM can be completely solidified (around 5h see Figure 14 (c)). In between these two moments, the latent heat sub-heat exchanger plays an important part of the instantaneous total energy transfer.

The sharp decrease in the predicted outlet temperature around 5 h (Figure 14 (c)) occurs at the time the latent sub-heat exchanger model predicts the PCM to have solidified at the inlet of the heat exchanger. Since the latent sub-heat exchanger model only considers latent heat, complete solidification at the inlet results in a part of the heat exchanger becoming thermally inactive and therefore the predicted heat transfer rate reduces. The result is a sharp drop in the predicted outlet temperature until the model predicts complete solidification when the predicted outlet temperature reverts to the outlet temperature of the sensible sub heat exchanger.

The reason for the sharper decline in outlet temperature could be found in the assumptions made when deriving the latent sub-heat exchanger model. This model divides the storage material in infinitesimally thin local slices and neglects the heat transfer between these slices. As a result, the difference in local liquid fraction is overestimated by the model which leads to a sharper decrease in temperature than what is measured. Improving the model prediction would thus require altering the latent sub-heat exchanger model.

Besides the outlet temperature of the HTF, the model also predicts the energy stored in total and in each of the separate sub-heat exchangers. Figure 15 shows the integrated measured and integrated efflux of energy as well as the stored energy in the sub-heat exchangers. Note that the stored energy or the total internal energy change of the system is not measured as the considerable energy losses do not allow to use the efflux of energy as an estimate for the stored energy. As a result, the internal energy change prediction is higher than the measured efflux: the internal energy change is the result of both heat loss and the energy transferred by the HTF. The predicted efflux is higher than the measured efflux (by about 4.6%) until it starts decreasing. This decrease occurs due to the complete solidification predicted by the latent sub-heat exchanger model. After this point, losses are dominant in the model prediction.

Similar to the outlet temperature of the sub-heat exchangers, the relative importance of each sub-heat exchanger is visible in Figure 15. At first, the internal energy change of the HTF is dominant, after which the sensible sub-heat exchanger takes over. The latent heat exchanger is dominant until the solidification ends. At this point, the internal energy of the system hardly changes and steady heat losses are predicted.

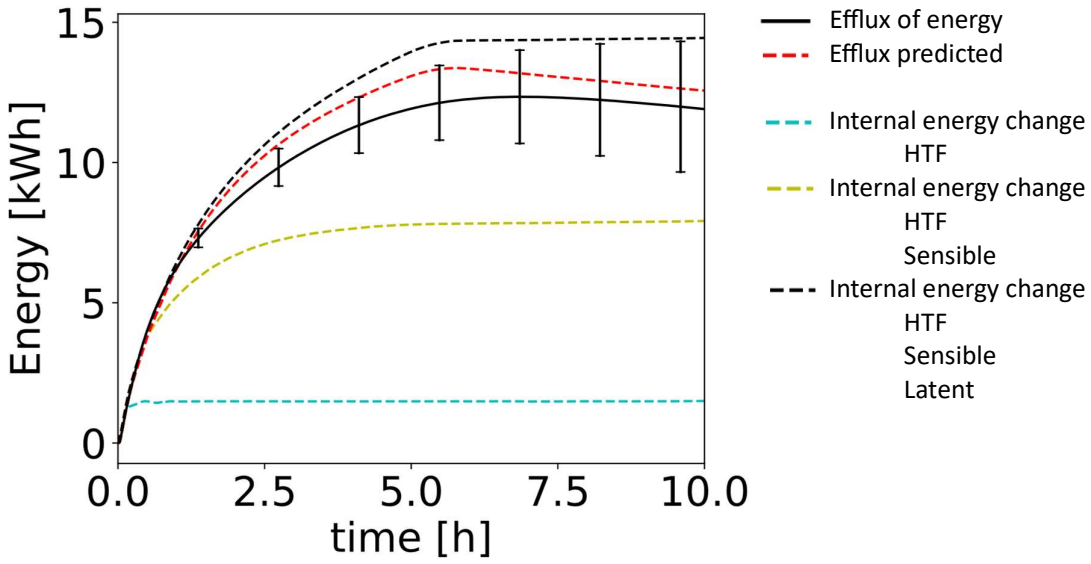

Figure 15: Measured and predicted total efflux of energy as well as the predicted internal energy change for the HTF, HTF and sensible heat and all sub-heat exchangers as a function of time for the solidification case with a volumetric flow rate of 0.5 m³/h and a temperature difference of 25 K.

Figure 16 shows the result for all six solidification experiment types while Table 8: Maximal absolute difference and maximum of the average temperature difference between the measured and predicted outlet temperature for the solidification experiments. Table 8 summarizes the maximal and average deviation between predicted and measured outlet temperature. The trends are similar for all six cases: the predicted outlet temperature is quite close to the measured outlet temperature up to the sharp decline in the predicted outlet temperature, with maximal deviations between 6.4 K for the 0.5 m³/h 25 K case and 1.9 K for the 0.5 m³/h 10 K. The average error on the predicted outlet temperature is larger for the lower HTF volume flow rate. Whether this is due to the larger temperature difference between the inlet and outlet or due to a larger modeling error cannot be established.

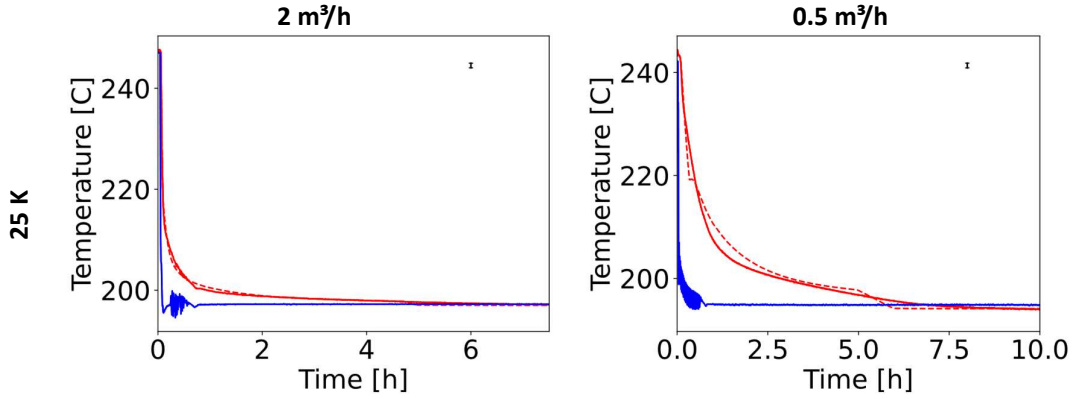

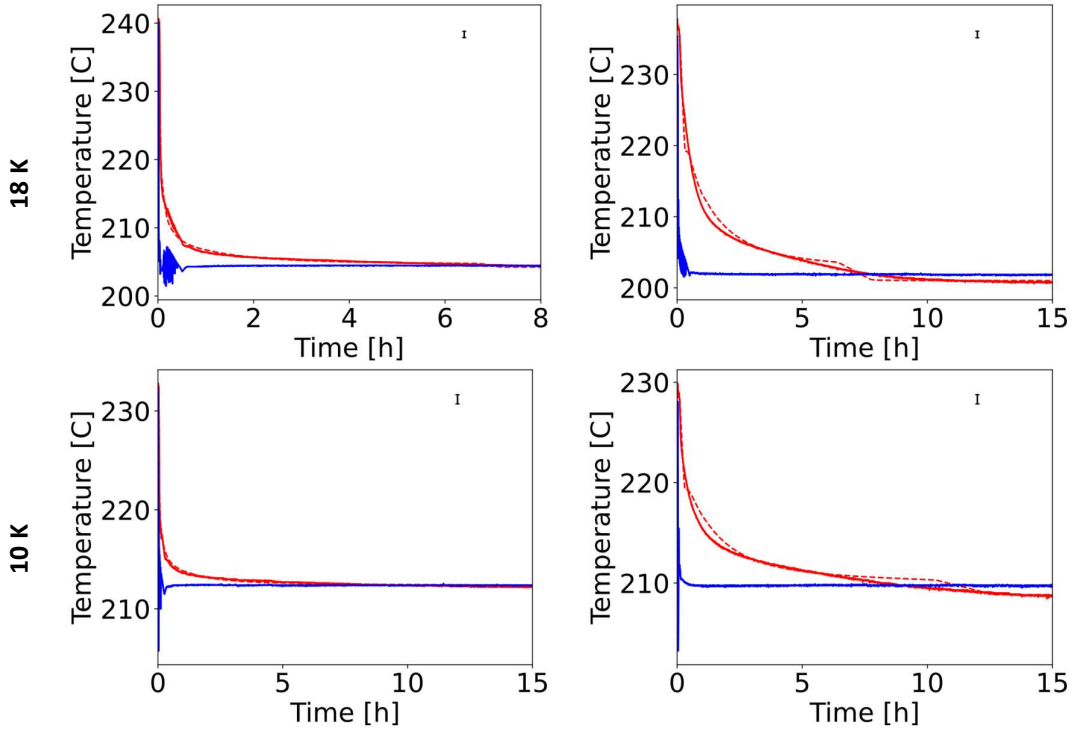

Figure 16: Measured HTF inlet (red) and outlet (blue) temperature and predicted HTF outlet temperature (black) for the 6 experiment types for the solidification experiments. Error bars on the top right hand corner of each figure are added as a reference.

Table 8: Maximal absolute difference and maximum of the average temperature difference between the measured and predicted outlet temperature for the solidification experiments.

		25 K		**18 K**		**10 K**	
2 m³/h	Max	2.2 K	Max	3.5 K	Max	3.2 K
	Average	0.3 K	Average	0.14 K	Average	0.1 K
0.5 m³/h	Max	6.4 K	Max	4.4 K	Max	1.9 K
	Average	0.8 K	Average	0.4 K	Average	0.3 K

4.4. Melting

As with the solidification cases, the melting experiment with a volumetric flow rate of 0.5 m³/h and a temperature difference of 25 K is first discussed. Figure 17 shows the measured and predicted in- and outlet HTF temperatures. As in the solidification experiments, the prediction obtains a good fit until the model predicts complete melting at the inlet around 3 hours into the experiment (see Figure 17 c). Unlike with the solidification case, the predicted rapid increase in outlet temperature does seem to occur at an inflection point in the outlet measured HTF temperature. However, the increase is much more gradual in the experimental results.

Figure 17 (b) shows the first 1.5 hours of charging. As in the solidification case, the HTF sub-heat exchanger model only plays a significant role at the start of the experiment, after which the sensible heat exchanger takes over, followed by the latent sub-heat exchanger.

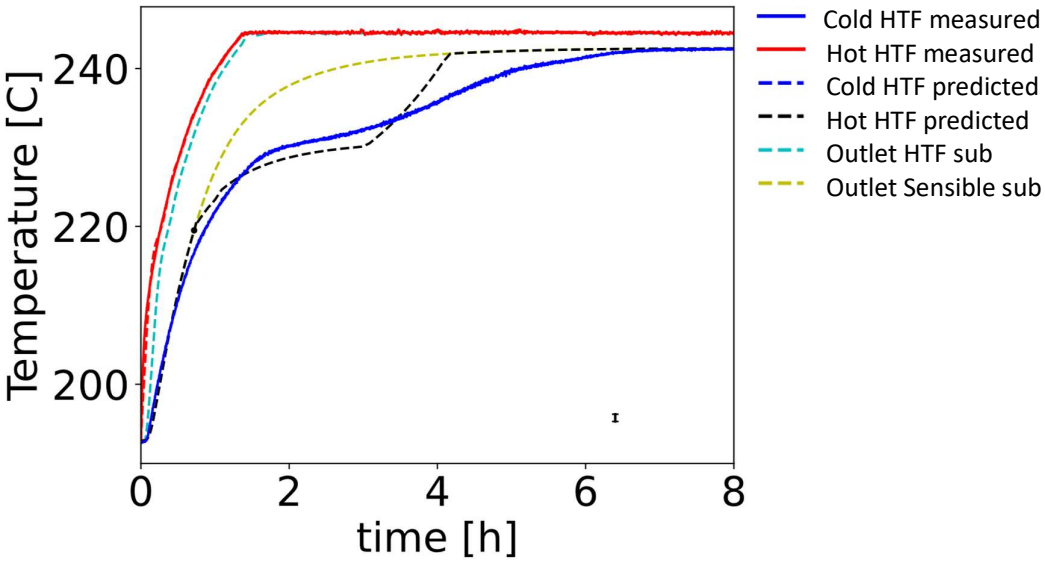

(a) Complete melting experiment

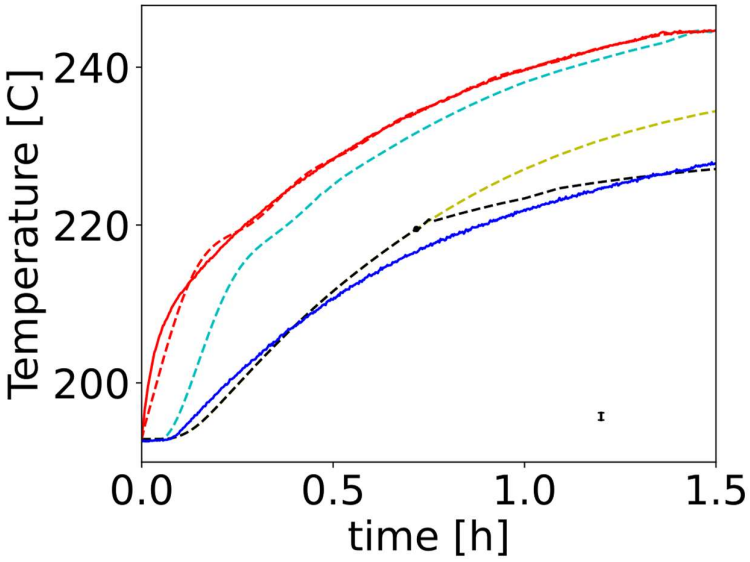

(b) Close-up of the 1.5 h of melting

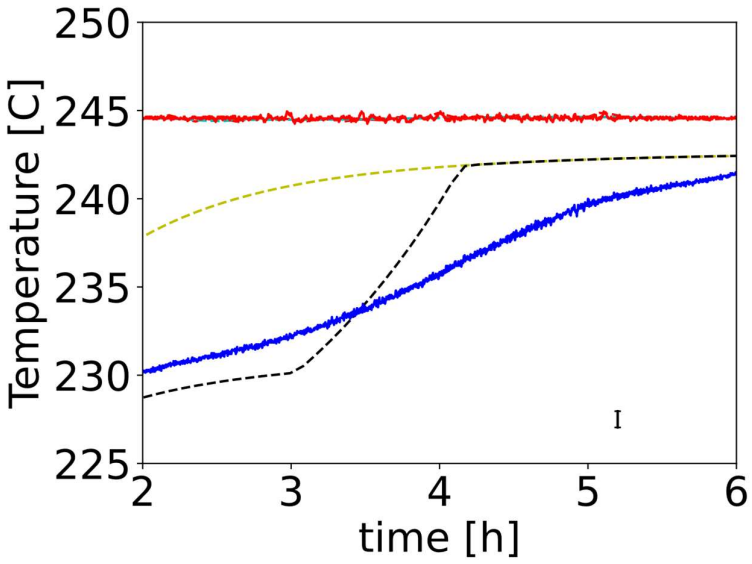

(c) Close-up of the predicted outlet temperature increase between 2and 6 h

Figure 17: Comparison of measured HTF temperatures with the predicted HTF temperatures with additional results for each of the sub-heat exchangers for the melting case with a volumetric flow rate of 0.5 m³/h and a temperature difference of 25 K.

The stored energy of each sub-heat exchanger as well as the predicted and measured efflux of energy are shown on Figure 18. Due to the gradually increasing inlet temperature, all sub-heat exchangers have a change in internal energy until the inlet HTF temperature stabilizes. Due to the faster increase in the predicted HTF outlet temperature, the total efflux of energy is underestimated by the model by 8.6%.

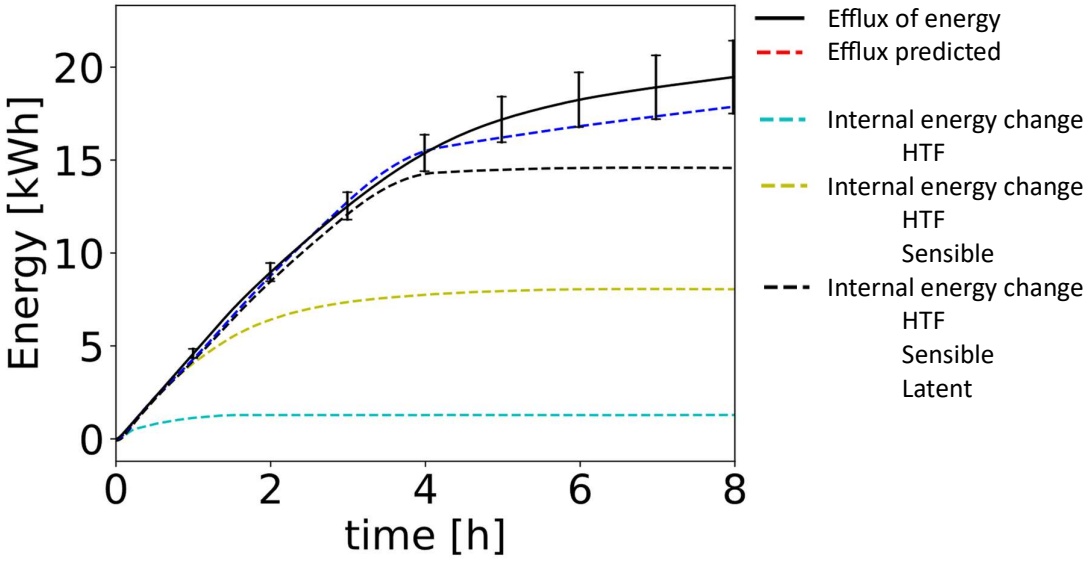

Figure 18: Measured and predicted total efflux of energy as well as the predicted internal energy change for the HTF, HTF and sensible heat and all sub-heat exchangers as a function of time for the melting case with a volumetric flow rate of 0.5 m³/h and a temperature difference of 25 K.

Figure 19 takes a look at the predicted and measured HTF outlet temperature for all the experiments with Table 9 quantifying the maximal and average deviation. The model predictions find reasonable

agreement with all cases up to the sharp increase in the predicted outlet temperature. The model agrees well again once a steady-state is reached, which corresponds with the heat loss prediction. As with the solidification cases, the 2 m³/h cases seem to have better model agreement than the cases with a volume flow rate of 0.5 m³/h.

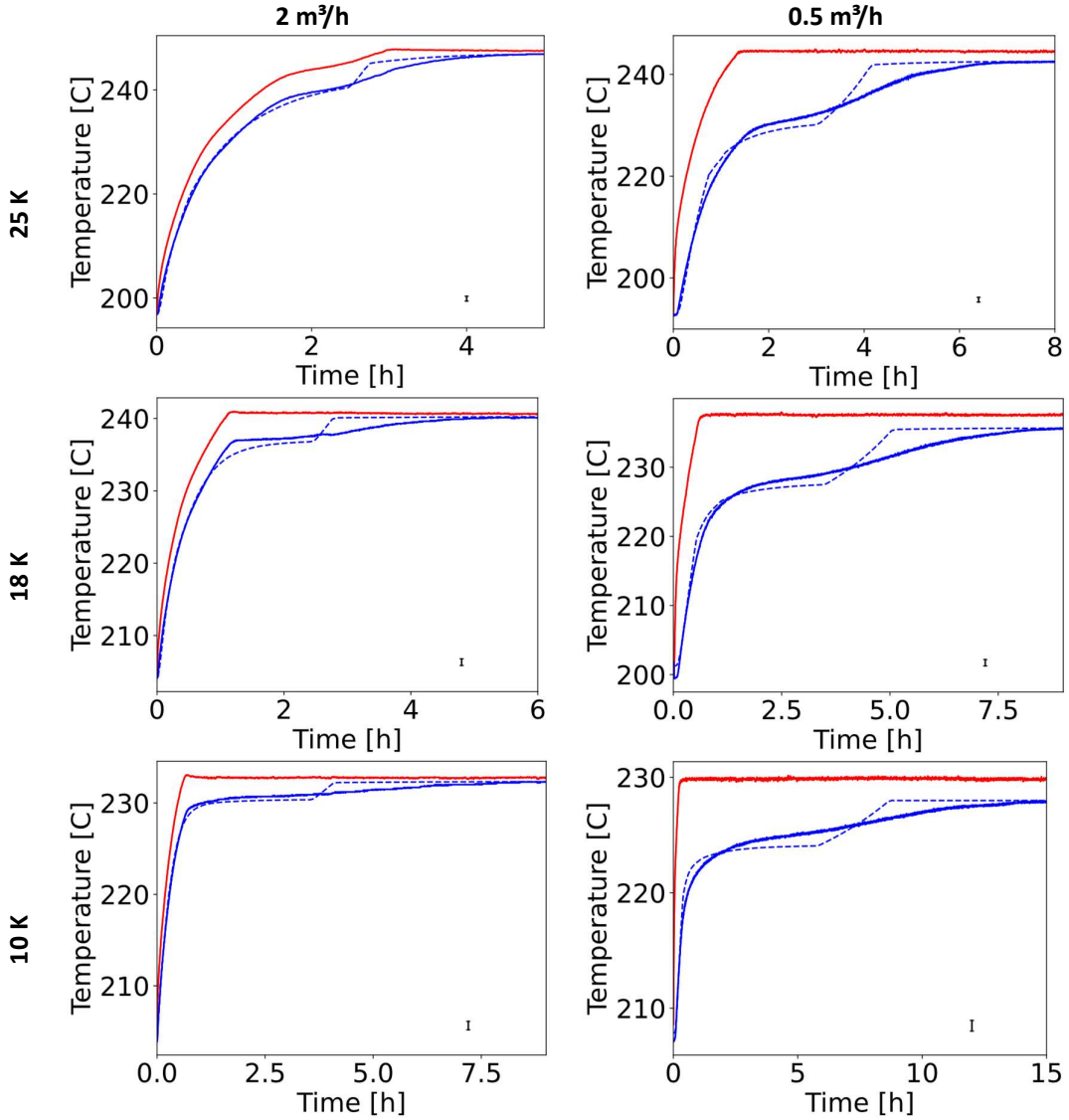

Figure 19: Measured HTF inlet (red) and outlet (blue) temperature and predicted HTF outlet temperature (blue dashes) for the 6 experiment types for the melting experiments. Error bars on the bottom right hand corner of each figure are added as a reference.

Table 9: Maximal and average absolute difference between the measured inlet temperature and the approximation using 40 terms in the Fourier series for the melting experiments.

		25 K		18 K		10 K	
2 m³/h	Max	2.8 K	Max	2.3 K	Max	1.3 K
	Average	0.4 K	Average	0.6 K	Average	0.4 K
0.5 m³/h	Max	5.4 K	Max	3.9 K	Max	1.9 K
	Average	1.2 K	Average	1 K	Average	0.7 K

5. Model comparison, limitations and future recommendations

The modeling approach is compared on to two commonly used methods in literature and described in the introduction: computational fluid dynamics and homogeneous diffusion only models (Table 10). The first metric which can be looked into is the calculation speed. Pointner et al. [32] compared the prediction of local PCM temperature for different implementations of homogeneous diffusion only models for the flat plate heat exchanger studied in this paper. The calculation time ranged from 12,31 s to 22020 s depending on the number of elements used. This calculation time can be scaled to take into account the hardware used for this paper (Intel® Core™ i5-1135G7 @ 2.40GHz) to 6.15 s and 10993 s. The semi analytical approach requires 0.16 s to calculate the output of the system at any given time. The semi-analytical approach is thus much faster than homogeneous diffusion only models which in turn are much faster than CFD models.

The next comparison metric is the maximum size of a system which can feasibly be calculated. As described in the introduction, the required element size and time step are a constraint to the maximal system size which can be calculated using CFD. The homogeneous diffusion only models require much less elements, can use larger time steps and only solve a single equation and are therefore capable of calculating full system sizes. However, the calculation time does scale with the number of elements used which in turn scales with the size of the system. The computational complexity of the semi-analytical approach does not scale with the size of the system and therefore it is capable of predicting the output of very large systems.

The third metric is the accuracy of the prediction. In this category, CFD models have a high potential for accurate predictions of LTES systems with for example the work of Tay et al. [49] where close agreement was found between the outlet HTF temperature predicted and measured. The homogeneous diffusion models studied by Pointner et al. [32] have average deviations of about 1.1 °C in local PCM temperature which is comparable to the average deviations reported for the semi-analytical approach. However, the trend in the prediction of the homogeneous diffusion only models closely follows the trend in the experimental measurements while the semi-analytical approach predicts a to sharp end to the charging process.

The final metric in Table 10 is the requirement for known sub-models and heat loss parameters. Note that of the comparable design methods only CFD models do not have this limitation, while homogeneous diffusion only models employ similar sub models for effective thermal conductivity as is done in the present paper. CFD models on the other hand are limited in maximum system size. Therefore, a hybrid approach where CFD is used to calibrate the local models such as the ones reported in [50, 51] while the integration approach is used to model the total system can alleviate the issues of both modeling strategies.

Table 10: Comparison between modeling options for latent thermal energy storage heat exchangers.

	CFD	Homogeneous diffusion only models	Semi-analytical approach
Speed	---	+	++
Max. system size	--	+	++
Accuracy	++	+	-
Need for sub models	++	-	-

A limitation of the presented approach is the reliance on a set of assumptions such as the parallel channel approach or the state series approach. Furthermore, both the sensible and latent heat models assume one of two extreme behaviors for the storage material as a function of the spatial coordinate : either the local state of the storage material is the same throughout the system (i.e. a lumped

approach) or the local state of the storage material is only a function of the local HTF state. The accuracy of these assumptions depends on the operation of the tested storage system. Therefore, the present model validation only applies to LTES systems which are similar to the one presented here.

The limitation of the applicability of the presented models to similar systems poses a question: what is a similar system? The semi-analytical modeling approach can help answer these question based on the used sub-models [34, 35, 45]. The resulting characteristics of the present system are summarized in Table 11 and depicted graphically on Figure 20.

Table 11: Characteristics of the flat plate LTES system for the different operating points.

		25 K	18 K	10 K
Energy balance				
% HTF energy		9.2 %	7.8 %	5.5 %
% Container energy		11.4 %	9.7 %	6.8 %
% Sensible PCM		34.2 %	29.1 %	20.4 %
% Latent PCM		45.2 %	54.4 %	67.3 %
HTF time constant τ_{HTF}				
0.5 m³/h			6 min	
2.0 m³/h			1.5 min	
Sensible time constant τ_{sens}				
0.5 m³/h	Liquid	0.87 hr	0.91 hr	0.98 hr
	Solid		2.28 hr	
2.0 m³/h	Liquid	0.74 hr	0.78 hr	0.85 hr
	Solid		2.16 hr	
Inlet phase change time t_0				
	Melting	1.4 hr	2.0 hr	4.0 hr
	Solidification	3.9 hr	5.4 hr	9.7 hr
Dimensionless size γ				
0.5 m³/h	Melting	0.7	0.67	0.61
	Solidification		0.25	
2.0 m³/h	Melting	0.174	0.167	0.154
	Solidification		0.06	
Losses / transfer to storage				
solidification			3.13 %	
melting		2.06 %	2.17 %	2.38 %

The first set of characteristics is the relative contribution to the total stored energy (calculated as Equation (54)) of each of the sub-heat exchangers. Note that the sensible sub-heat exchanger contains both the heat of the container and the sensible heat in the PCM. The relative contribution changes with the initial and inlet condition as larger temperature changes result in a larger contribution of the sensible heat.

The second characteristic is the time constant for the HTF sub-heat exchanger model τ_{HTF} or the total volume of the HTF divided by the volume flow rate. The time constant gives an order of magnitude estimation for the duration of the initial plateau in the outlet temperature as the HTF within the heat exchanger is displaced.

The third characteristic is the sensible time constant which is based on the sensible sub-models reported in [45]. The most simplified sensible sub-model assumes a uniform storage system temperature and a constant heat transfer resistance. In this case, the temperature response corresponds with a first order system with a time constant defined as Equation (64).

$$\tau_{sens} = \frac{MC_{sens}}{\dot{m}c_p\left(1 - \exp\left(-\frac{A}{R_{equiv}\dot{m}c_p}\right)\right)} \tag{64}$$

With
- MC_{sens} The total sensible heat capacity of the PCM and container material.
- A The heat transfer surface area
- R_{equiv} The equivalent thermal resistance (determined here as Equation (66))

The sensible time constant only has a limited variation as a function of the volume flow rate. This is a result of the low heat exchanger effectiveness $\left(1 - \exp\left(-\frac{A}{R_{equiv}\dot{m}c_p}\right)\right)$ since for low effectiveness values the decrease in effectiveness with a higher mass flow rate negates the increase in thermal capacity of the heat transfer fluid.

The difference in sensible time constant between the liquid and solid phase is due to the natural convection in the case of a liquid storage material. This natural convection is also the reason for the variation in time constant as a function of driving temperature difference. The natural convection significantly increases the heat transfer rate and reduces the time constant by a factor of almost three.

There are two characteristics reported for the latent heat sub model: the inlet phase change time t_0 and the dimensionless size of the system γ. The former is the time required for complete phase change if the HTF temperature is at the inlet temperature throughout the heat exchanger. This metric is based on the latent sub-heat exchanger model described in Section 3.3.3. The dimensionless size multiplied with the inlet phase change time gives the additional time required for the system to obtain complete phase change after phase change at the inlet is completed. It is defined according to [35] as Equation (65).

$$\gamma = \frac{M_{pcm}h_{lat}\,A}{\dot{m}c_p t_0 \Delta\overline{\mathrm{T}}} \tag{65}$$

The inlet phase change time varies as a function of inlet temperature and whether the PCM is melting or solidifying but is independent of the HTF volume flow rate. The volume flow rate has an influence on both the temperature program of the HTF in the heat exchanger and the convective heat transfer coefficient. However the inlet HTF temperature is of course not a function of the volume flow rate and the convective heat transfer coefficient of the HTF is assumed to be constant. As a result, the volume flow rate does not influence the predicted inlet phase change time.

The difference between the melting and solidification case is the result of the natural convection in the phase change material. Similarly as with the sensible system time constant, the presence of natural convection reduces the phase change time by almost a factor of three.

The temperature difference has a larger effect on the inlet phase change time than on the sensible time constant. In the sensible model, the driving temperature also increases the sensible heat and as a result a higher driving temperature difference does not result in a shorter phase change time. In the latent heat model however, the larger temperature difference increases the heat transfer rate while not affecting the total latent heat. As a result, the inlet phase change time is approximately inversely proportional to the inlet temperature difference. For the melting cases, the inlet temperature difference also increases the natural convection in the PCM further reducing the phase change time.

The final parameter describing the latent heat in the system is the dimensionless size. It is inversely proportional to the volume flow rate in the system. The effect of the driving inlet temperature is partially negated by the inlet phase change time being inversely proportional to the inlet temperature difference. The remaining difference is due to the effect of natural convection.

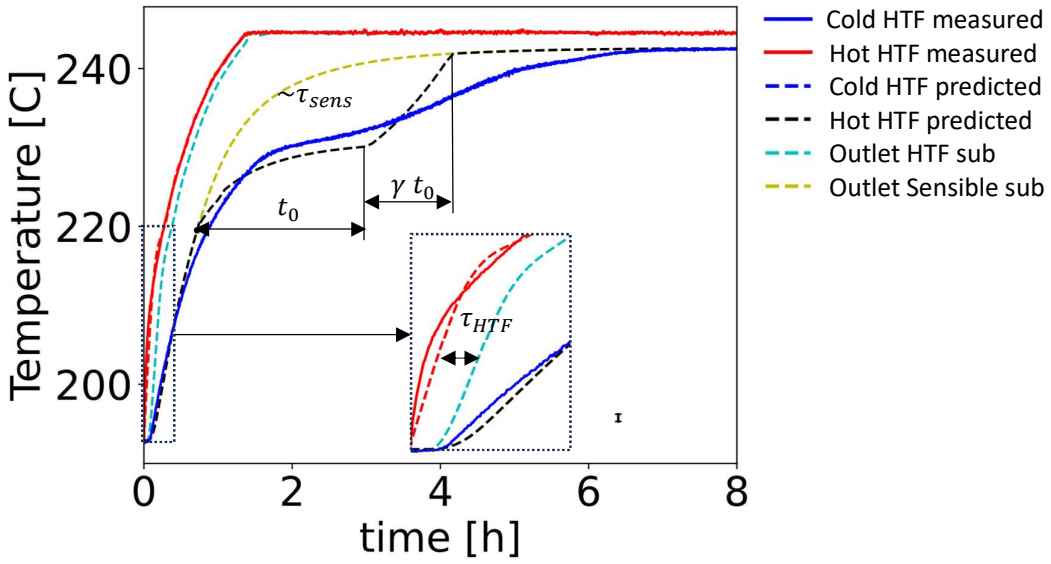

(a) Time constants.

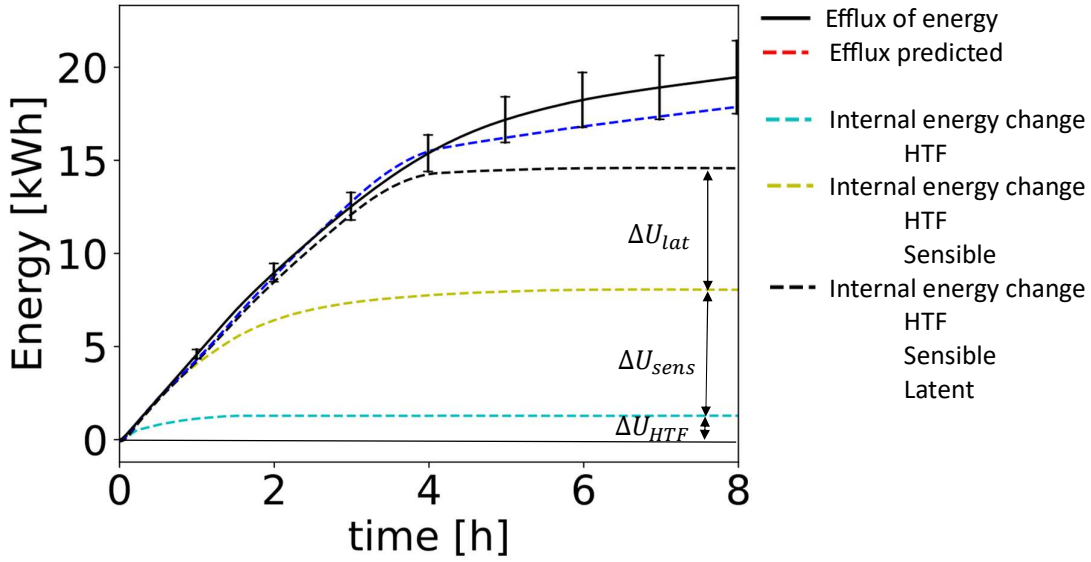

(b) Stored energy and integrated efflux of error.

Figure 20: System parameters reported in Table 11 for the melting case with a volumetric flow rate of 0.5 m³/h and a temperature difference of 25 K.

6. Conclusion

The present paper proposes a computationally efficient model for LTES heat exchangers. The model is based on previously published sub-models for sensible- and latent-heat-only storage systems. The models are combined based on a space-series-approach, which connects the sub-heat exchangers in series. The key novelty of the present paper is the application of the method to an LTES plate heat exchanger for which a large data set of melting and solidification experiments are available. Furthermore, heat losses are included in the model, which was not done in previously published work.

The model predicts the HTF outlet temperature with an average deviation of maximal 1.2 K. The greatest difference between predicted and measured values are found in the final (dis)charging stage, where the experimental data show a gradually decreasing energy transfer, while the model predicts a sharp decrease in the heat transfer. Specific model assumptions and simplifications contributing to this deviation require further investigation to improve the predictive capabilities of the model. Despite of these limitations, the proposed model accurately predicts the outlet temperature in the majority of the experiments with a minimal computational effort. Furthermore, the computational effort does not increase with the size of the system as is the case for finite volume methods. As a result, the proposed modeling method provides a valuable tool for sizing large-scale systems offering a practical solution for designing LTES-systems where computational efficiency is crucial.

Nomenclature

Symbol	Unit	Meaning
A	m^2	Surface area, used as an independent variable in the heat transfer fluid integration methods.
a_i and b_i	-	Fourier series coefficients.
c_{CON}	J/kgK	Specific heat capacity of the container material.
c_{HTF}	J/kgK	Specific heat capacity of the heat transfer fluid.
c_p	J/kgK	Specific heat capacity under constant pressure
c_{PCM}	J/kgK	Specific heat capacity of the phase change material.
D	m	Depth of the single parallel channel
g	m/s^2	Gravitational acceleration
h	W/m^2K	Convective heat transfer coefficient.
h_{in}	J/kg	Specific enthalpy of the heat transfer fluid at the inlet
h_{out}	J/kg	Specific enthalpy of the heat transfer fluid at the inlet
h_{lat}	J/kg	Latent heat of phase change.
k	W/mK	Thermal conductivity
L	m	Length of the single parallel channel
$\dot{m}$	kg/s	Mass flow rate
$\dot{m}_{HTF}$	kg/s	Mass flow rate of a single parallel channel
m_{HTF}	kg	Mass of the heat transfer fluid.
m_{ij}	-	Thermal quadrupole function.
M_{CON}	kg	Total mass of container material in the system.
m_{ii}^{CON}	-	Thermal quadrupole function for the container material.
m_{ii}^{PCM}	-	Thermal quadrupole function for the phase change material volume.
M_{ij}	-	Combined thermal quadrupole function.
M_{PCM}	kg	Total mass of PCM in the system.
MC_{sens}	J/K	Total thermal mass of the sensible sub-heat exchanger
$n_{Fourier}$	-	Number of terms in the Fourier series approximation for the inlet temperature.
p	Hz	Laplace parameter
r_{HTF}	[-]	Modeling parameter expressing the fraction of the heat transfer fluid which is modelled as a perfectly mixed vessel.
Ra_W	-	Rayleigh number based on the width of the PCM channel.
R_{equiv}	Km^2/W	Equivalent heat transfer resistance.
$\dot{Q}_{amb}$	W	Heat loss modelled in the single parallel channel approach.
$\dot{q}_{amb}$	W/m	Heat loss per unit of length in the single parallel channel approach.
$\dot{Q}_{loss}$	W	Heat loss
T	s	Time
t_0		

t_{end}	s	End time of the experiment
t_{con}	s	Time for the phase change front to reach the edge of the phase change material volume taking only latent heat into account, neglecting natural convection and under the inlet heat transfer fluid temperature.
T_{end}	°C	Final temperature of the system
T_{HTF}	°C	Heat transfer fluid temperature.
T_{HTF}^{out}	°C	Heat transfer fluid temperature at the outlet of the heat transfer fluid sub heat exchanger
T_{in}	°C	Inlet temperature
T_{ini}	°C	Initial temperature
T_{out}	°C	Outlet temperature
T_{pc}	°C	Phase change temperature
T_{sens}^{out}	°C	Heat transfer fluid temperature at the outlet of the sensible sub heat exchanger
u	J/kg	Specific internal energy
U	J	Internal energy
U_{loss}	W/m²K	Heat loss
U_{HTF}	J	Internal energy of the heat transfer fluid
U_{CON}	J	Internal energy of the container material
U_{lat}	J	Internal energy of the latent heat sub heat exchanger.
U_{PCM}	J	Internal energy of the phase change material
U_{PCM}^{sens}	J	Sensible heat of the phase change material
U_{sens}	J	Internal energy of the latent heat sub heat exchanger
UA_{loss}^{avg}	W/K	Overall heat loss of the system determined by the energy balance.
UA_{loss}^{end}	W/K	Overall heat loss of the system determined by the end temperature differences.
V_{HTF}	m³	Volume of the heat transfer fluid.
V_{CON}	m³	Volume of the container material.
V_{PCM}	m³	Volume of the phase change material.
W	m	Total width of the single parallel channel.
w	m	Width.
w_{HTF}	m	Width of the heat transfer fluid channel in the single parallel channel.
w_{CON}	m	Width of the container material in the single parallel channel.
w_{PCM}	m	Width of the phase change material in the single parallel channel.
x	[1,0,0] m	Coordinate axis as defined in Figure 6.
y	[0,1,0] m	Coordinate axis as defined in Figure 6.
z	[0,0,1] m	Coordinate axis as defined in Figure 6.
_(x,y,z,t)		As a function of x, y, z position and time.
_(y,t)		As a function of y position and time. Integrated (extensive properties) or averaged (intensive properties) over the x and z coordinate.
$\tilde{a}$		Laplace transform of the variable a.
$\tilde{a}_L$		Laplace transform of the variable a at the left hand side of a body with one dimensional conduction.
$\tilde{a}_R$		Laplace transform of the variable a at the right hand side of a body with one dimensional conduction.

Greek

α	m²/s	Thermal diffusivity of the material.

β	1/K	Coefficient of thermal expansion.
γ		Dimensionless size of the latent heat exchanger.
ε_{ccon}	J/kgK	Error estimate for the specific heat capacity of the container material.
ε_{cpcm}	J/kgK	Error estimate for the specific heat capacity of the PCM material.
ε_E	W	Error estimate for the efflux of energy as a function of time
$\varepsilon_{\dot{V}\,\%}$	-	Fractional error on the measured volume flow rate.
$\varepsilon_{\Delta E}$	J	Error estimate for the integrated efflux of energy.
$\varepsilon_{\Delta T}$	K	Error on the measured temperature difference
$\varepsilon_{\Delta U}$	J	Error estimate for the stored energy.
$\varepsilon_{\rho c\,\%}$	-	Fractional error on the product of the density and the specific heat capacity of the heat transfer fluid.
$\Delta\mathrm{E}$	J	Integrated efflux of energy.
$\Delta\mathrm{T}$	°C	Temperature difference between the local heat transfer fluid and the phase change temperature.
$\Delta\bar{T}$	°C	Time averaged temperature difference between the local heat transfer fluid and the phase change temperature.
ΔT_{inlet}	°C	Temperature difference between the heat transfer fluid and the phase change temperature at the inlet of the
ΔT_{liq}	°C	Temperature difference for the liquid phase change material.
ΔT_{tot}	°C	Temperature difference between the initial and final temperature for an experiment.
ΔT_{sol}	°C	Temperature difference for the solid phase change material.
ΔU	J	Internal energy change for the system if the temperature is changed from the initial to the final temperature.
θ	-	Dimensionless temperature based on the temperature difference between the inlet and the initial temperature.
θ_{amb}	-	Dimensionless ambient temperature.
θ_{HTF}	-	Dimensionless temperature of the local heat transfer fluid temperature.
$\theta_{L\,or\,R}^{CON}$	-	Dimensionless temperature of the local container temperature on the left or right hand side.
$\theta_{L\,or\,R}^{PCM}$	-	Dimensionless temperature of the local phase change material temperature on the left or right hand side.
λ	-	Liquid fraction.
λ_{loc}	-	Liquid fraction averaged over the x and z coordinates as a function of time and the local average temperature difference between the heat transfer fluid and the phase change temperature.
ρ_{CON}	kg/m³	Density of the container material.
ρ_{HTF}	kg/m³	Density of the heat transfer fluid.
ρ_{PCM}	kg/m³	Density of the phase change material.
τ_{FO}	s	Time constant for the first order function fitting of the inlet temperature measured time signal.
τ_{sens}	s	Time constant for the sensible heat sub heat exchanger.
ν	m²/s	Kinematic viscosity.
φ	W/m²K	Heat flux per unit of temperature difference
φ_{amb}	W/m²K	Heat flux to the ambient per unit of temperature difference.
$\varphi_{L\,or\,R}^{CON}$	W/m²K	Heat flux per unit of temperature difference on the left or right hand side of the container material.

$\varphi_{L\ or\ R}^{PCM}$	W/m²K	Heat flux per unit of temperature difference on the left or right hand side of the phase change material volume.

Abbreviations

Symbol	Meaning
CFD	Computational Fluid Dynamics
HTF	Heat Transfer Fluid
LTES	Latent Thermal Energy Storage
PCM	Phase Change Material
STES	Sensible Thermal Energy Storage
TES	Thermal Energy Storage

Appendix A: Error analysis

1. Constant material properties uncertainty assessment

In order to assess the effect of the constant properties assumption on the overall model accuracy, two concepts will be used: the overall energy balance of the system and an equivalent thermal resistance. The analysis of the energy balance is summarized in Table 12. The largest share of the internal energy is the storage material with 79.4% of the heat stored of which 45.2% is latent heat. The container contains only 11.4% of the heat while the HTF contains 9.2% of the internal energy change. The total error on the internal energy change for a temperature change of 50 °C is estimated as 0.7%.

Table 12: Percentual contribution to the energy balance of the system for a temperature change of 50 °C including the latent heat.

Component	Share in energy balance	% variation ± 25 °C
PCM	79.4%	± 0.3%
Latent heat	45.2%	
Sensible heat liquid	16.2%	
Sensible heat solid	17.9%	
Container	11.4 %	± 0.01 %
HTF	9.2 %	± 0.4 %
	Total	**± 0.7 %**

The second metric is a representative thermal resistance R_{equiv} between the HTF and the storage material, as defined by Equation (66). The convective heat transfer coefficient for this heat exchanger was previously estimated as 200 W/mK (no uncertainty value was provided and therefore a 20 % uncertainty is assumed). The thermal conductivity of the wall and PCM are found in respectively Table 2 and Table 1, while the PCM and wall width are given in the experimental setup description.

$$R_{equiv} = \left(\frac{1}{h} + \frac{w_{wall}}{k_{wall}} + \frac{w_{PCM}}{k_{PCM}}\right)^{-1} \tag{66}$$

With
- h the convective heat transfer coefficient in the PCM
- w_{wall} The wall width
- k_{wall} The thermal conductivity of the wall
- w_{PCM} The PCM width
- k_{PCM} The thermal conductivity of the PCM

The PCM layer contributes 94.5% to the equivalent thermal resistance, while the convective heat transfer in the HTF contributing 5.4%. The wall only contributes 0.1% to the total thermal resistance. The impact of the uncertainty on the thermal conductivity of the PCM is only 0.1%, while the impact for the uncertainty of the steel is negligible.

2. Error analysis

The efflux of energy is determined as Equation (53). The error on the estimated efflux of energy is determined as (68) according to the measurement error theory of Taylor [52]. The fractional error on the volume flow rate $\varepsilon_{\dot{V}\,\%}$, the fractional error on the product of the density and the sensible heat $\varepsilon_{\rho c\,\%}$ and the error on the temperature difference $\varepsilon_{\Delta T}$ is given in respectively Table 5, Table 3 and Table 5.

$$\Delta E = \int_0^t \dot{V}_{HTF}(t)\rho_{HTF}c_{HTF}\left(T_{out}(t) - T_{in}(t)\right)dt \qquad \text{See (53)}$$

$$\varepsilon_E = \sqrt{\begin{array}{c}\left((\varepsilon_{\dot{V}\,\%})^2 + \left(\varepsilon_{\rho c\,\%}\right)^2\right)\left(\dot{V}_{HTF}(t)\rho_{HTF}c_{HTF}\left(T_{out}(t) - T_{in}(t)\right)\right)^2 \\ +(\varepsilon_{\Delta T}\dot{V}_{HTF}(t)\rho_{HTF}c_{HTF})^2\end{array}} \qquad (67)$$

$$\varepsilon_{\Delta E} = \int_0^t \varepsilon_E\, dt \qquad (68)$$

The total stored energy is determined by Equation (54). The chain rule is used to determine the resulting error from to the error on the temperature ε_T (1.5 °C according to Table 5) and the error on the material properties (product of density and sensible heat of the HTF $\varepsilon_{\rho c\,\%}$ from Table 3, latent heat $\varepsilon_{h_{lat}}$ and specific heat capacity of the PCM ε_{cpcm} from Table 2 and error on the steel specific heat capacity ε_{ccon} from Table 1). Note that the phase change temperature is assumed to be in the middle between the initial and final temperature resulting in an averaged specific heat capacity for the PCM.

$$\Delta U = (V_{HTF}\rho_{HTF}c_{HTF} + M_{CON}c_{CON})\Delta T_{tot} + M_{PCM}(h_{lat} + c_{PCM}^{liq}\Delta T_{liq} + c_{PCM}^{sol}\Delta T_{sol}) \qquad \text{See (54)}$$

$$\varepsilon_{\Delta U} = \sqrt{\begin{array}{c}\left[V_{HTF}\rho_{HTF}c_{HTF} + M_{CON}c_{CON} + \frac{M_{PCM}\left(c_{PCM}^{liq} + c_{PCM}^{sol}\right)}{2}\right]^2 {\varepsilon_{\Delta T}}^2 + \\ [M_{CON}\varepsilon_{ccon}\,\Delta T_{tot}]^2 + \\ \left[M_{PCM}\varepsilon_{cpcm}\,\Delta T_{tot}\right]^2 \\ \left[M_{PCM}\varepsilon_{h_{lat}}\right]^2 +\end{array}} \qquad (69)$$

The overall heat loss coefficient based on the efflux at the end of the experiment is defined as Equation (60). The error ε_{loss}^{end} on this estimation is determined as Equation (70).

$$UA_{loss}^{end} = \frac{\dot{m}c_p\left(T_{in}(t_{end}) - T_{out}(t_{end})\right)}{T_{end} - T_{amb}} \qquad \text{See (60)}$$

$$\varepsilon_{loss}^{end} = \sqrt{\left[\frac{\varepsilon_E(t_{end})}{T_{end} - T_{amb}}\right]^2 + \left[\frac{\dot{m}c_p\left(T_{in}(t_{end}) - T_{out}(t_{end})\right)}{(T_{end} - T_{amb})^2}\varepsilon_{\Delta T}\right]^2} \qquad (70)$$

$$UA_{loss}^{avg} = \frac{|\Delta E - \Delta U|}{t_{end}\left(\frac{1}{2}\,(T_{ini} + T_{end}) - T_{amb}\right)} \qquad (71)$$

$$\varepsilon_{loss}^{avg} = \sqrt{\left[\frac{\varepsilon_{\Delta E}}{t_{end}\left(\frac{1}{2}\,(T_{ini}+T_{end})-T_{amb}\right)}\right]^2 + \left[\frac{\varepsilon_{\Delta U}}{t_{end}\left(\frac{1}{2}\,(T_{ini}+T_{end})-T_{amb}\right)}\right]^2 + \left[\frac{|\Delta E-\Delta U|}{\left(t_{end}\left(\frac{1}{2}\,(T_{ini}+T_{end})-T_{amb}\right)\right)^2}\varepsilon_{\Delta T}\right]^2}$$

Acknowledgements

This research was partially funded by a FWO grant (1246924N) for junior postdoctoral research of the Research Foundation – Flanders, Belgium. The financial support is gratefully acknowledged.

Reference

[1] W. Beyne, I. T'Jollyn, S. Lecompte, L. F. Cabeza, and M. De Paepe, "Standardised methods for the determination of key performance indicators for thermal energy storage heat exchangers," *Renewable and Sustainable Energy Reviews,* vol. 176, p. 113139, 2023/04/01/ 2023, doi: https://doi.org/10.1016/j.rser.2022.113139.

[2] L. F. Cabeza, Mehling, M., *Heat and cold storage with PCM: An up to date introduction into basics and applications*. Springer-Verlag Berlin Heidelberg, 2008.

[3] S. E. Kalnæs and B. P. Jelle, "Phase change materials and products for building applications: A state-of-the-art review and future research opportunities," *Energy Build.,* vol. 94, pp. 150-176, 2015/05/01/ 2015, doi: https://doi.org/10.1016/j.enbuild.2015.02.023.

[4] E. Oro, A. de Gracia, A. Castell, M. M. Farid, and L. F. Cabeza, "Review on phase change materials (PCMs) for cold thermal energy storage applications," (in English), *Appl. Energy,* Review vol. 99, pp. 513-533, Nov 2012, doi: 10.1016/j.apenergy.2012.03.058.

[5] K. Couvreur, W. Beyne, R. Tassenoy, S. Lecompte, and M. De Paepe, "Characterization of a latent thermal energy storage heat

exchanger using a charging time energy fraction method with a heat loss model," *Applied Thermal Engineering,* vol. 219, p. 119526, 2023/01/25/ 2023, doi: https://doi.org/10.1016/j.applthermaleng.2022.119526.

[6] M. Esen, "Thermal performance of a solar-aided latent heat store used for space heating by heat pump," *Sol. Energy,* vol. 69, no. 1, pp. 15-25, 2000.

[7] M. S. B. Jahromi, V. Kalantar, and H. Samimi-Akhijahani, "Evaluation of performance, energy, and exergy analysis of a solar parabolic dish collector connected to a dryer with nanofluid and PCM," *Journal of Energy Storage,* vol. 98, p. 112969, 2024.

[8] R. Sampath and N. Zabaras, "An object oriented implementation of a front tracking finite element method for directional solidification processes," *International Journal for Numerical Methods in Engineering,* vol. 44, no. 9, pp. 1227-1265, 1999.

[9] V. R. Voller, "Numerical Methods for Phase-Change Problems," in *Handbook of Numerical Heat Transfer*: John Wiley & Sons, Inc., 2009, pp. 593-622.

[10] M. Lacroix and V. Voller, "Finite difference solutions of solidification phase change problems: transformed versus fixed grids," *Numerical Heat Transfer,* vol. 17, no. 1, pp. 25-41, 1990.

[11] V. Safari, H. Abolghasemi, and B. Kamkari, "Experimental and numerical investigations of thermal performance enhancement in a latent heat storage heat exchanger using bifurcated and straight fins," *Renewable Energy,* vol. 174, pp. 102-121, 2021/08/01/ 2021, doi: https://doi.org/10.1016/j.renene.2021.04.076.

[12] T. Shockner *et al.*, "Simultaneous close-contact melting on two asymmetric surfaces: Demonstration, modeling and application to thermal storage," *Int. J. Heat Mass Transf.,* vol. 232, p. 125950, 2024/11/01/ 2024, doi: https://doi.org/10.1016/j.ijheatmasstransfer.2024.125950.

[13] R. D. Selvakumar and A. K. Alkaabi, "Design and performance evaluation of a novel electrohydrodynamically enhanced PCM

heat sink," *Journal of Energy Storage,* vol. 94, p. 112375, 2024/07/30/ 2024, doi: https://doi.org/10.1016/j.est.2024.112375.

[14] H.-Y. Liu, B.-C. Qu, C.-M. Wu, and Y.-R. Li, "Numerical study of PCM melting performance in a rectangular container with various longitudinal fin structures," *Journal of Energy Storage,* vol. 94, p. 112529, 2024/07/30/ 2024, doi: https://doi.org/10.1016/j.est.2024.112529.

[15] K. Kansara, S. Singh, N. K. Dwivedi, and M. L. Khodachenko, "Investigating combined effects of varying gravity and heat flux direction on the melting dynamics of phase change material in space," *Acta Astronautica,* vol. 220, pp. 427-448, 2024/07/01/ 2024, doi: https://doi.org/10.1016/j.actaastro.2024.05.005.

[16] V. C. Midhun, M. Maroliya, and S. K. Saha, "Numerical investigation and optimisation of solid–solid phase change material composite-based plate-fin heat sink for thermal management of electronic package," *Applied Thermal Engineering,* vol. 248, p. 123183, 2024/07/01/ 2024, doi: https://doi.org/10.1016/j.applthermaleng.2024.123183.

[17] R. Akula, A. Minnikanti, and C. Balaji, "Pin fin-PCM composite heat sink solution for thermal management of cylindrical Li-ion battery," *Applied Thermal Engineering,* vol. 248, p. 123146, 2024/07/01/ 2024, doi: https://doi.org/10.1016/j.applthermaleng.2024.123146.

[18] H. Kumar, G. Singh, and A. Yadav, "Computational comparison of approaches based on geometrical orientation and gravity components in analysing the melting behaviour of thermal energy storage system," *Multiscale and Multidisciplinary Modeling, Experiments and Design,* 2024/06/21 2024, doi: 10.1007/s41939-024-00498-0.

[19] C. Yang *et al.*, "Numerical investigation and optimization of the melting performance of latent heat thermal energy storage unit strengthened by graded metal foam and mechanical rotation," *Renewable Energy,* vol. 227, p. 120537, 2024/06/01/ 2024, doi: https://doi.org/10.1016/j.renene.2024.120537.

[20] S. Baghaei Oskouei and Ö. Bayer, "Performance improvement in a vertical latent thermal energy storage tank with crossing heat transfer tubes," *Journal of Energy Storage,* vol. 88, p. 111504, 2024/05/30/ 2024, doi: https://doi.org/10.1016/j.est.2024.111504.

[21] M. A. Khuda, L. Yan, J. Khalesi, N. Sarunac, and C. Romero, "Energy and exergy analysis of a laboratory-scale latent heat thermal energy storage (LTES) using salt-hydrate in a staggered tube arrangement," *Journal of Energy Storage,* vol. 87, p. 111320, 2024/05/15/ 2024, doi: https://doi.org/10.1016/j.est.2024.111320.

[22] A. F. Khalaf, F. L. Rashid, M. A. Al-Obaidi, A. Ameen, and H. I. Mohammed, "Numerical investigation of the effect of an air layer on the melting process of phase change materials," *Materials for Renewable and Sustainable Energy,* 2024/05/14 2024, doi: 10.1007/s40243-024-00261-y.

[23] W. Ye and J. M. Khodadadi, "Effects of varying geometrical parameters on the melting performance of phase change materials within L-shaped shell-and-tube latent heat thermal energy storage units with radial eccentricity exhibiting prominent influence," *Journal of Energy Storage,* vol. 86, p. 111334, 2024/05/10/ 2024, doi: https://doi.org/10.1016/j.est.2024.111334.

[24] J. Vogel, M. Keller, and M. Johnson, "Numerical modeling of large-scale finned tube latent thermal energy storage systems," *Journal of Energy Storage,* vol. 29, p. 101389, 2020/06/01/ 2020, doi: https://doi.org/10.1016/j.est.2020.101389.

[25] J. Vogel and M. Johnson, "Natural convection during melting in vertical finned tube latent thermal energy storage systems," *Appl. Energy,* vol. 246, pp. 38-52, 2019/07/15/ 2019, doi: https://doi.org/10.1016/j.apenergy.2019.04.011.

[26] N. H. S. Tay, F. Bruno, and M. Belusko, "Experimental validation of a CFD and an ε-NTU model for a large tube-in-tank PCM system," *Int. J. Heat Mass Transf.,* vol. 55, no. 21, pp. 5931-5940,

2012/10/01/ 2012, doi: http://dx.doi.org/10.1016/j.ijheatmasstransfer.2012.06.004.

[27] M. Esen and T. Ayhan, "Development of a model compatible with solar assisted cylindrical energy storage tank and variation of stored energy with time for different phase change materials," *Energy Conversion and Management,* vol. 37, no. 12, pp. 1775-1785, 1996.

[28] M. S. B. Jahromi, V. Kalantar, M. Sefid, H. S. Akhijahani, and M. Iranmanesh, "Energy and exergy analysis of an unglazed transpired collector connected to a dryer with a porous plate and phase change material," *Journal of Energy Storage,* vol. 60, p. 106693, 2023.

[29] W. Beyne, K. Couvreur, I. T'Jollyn, S. Lecompte, and M. De Paepe, "Estimating the state of charge in a latent thermal energy storage heat exchanger based on inlet/outlet and surface measurements," *Applied Thermal Engineering,* vol. 201, p. 117806, 2022.

[30] I. Jmal and M. Baccar, "Numerical study of PCM solidification in a finned tube thermal storage including natural convection," *Applied Thermal Engineering,* vol. 84, pp. 320-330, 2015/06/05/ 2015, doi: https://doi.org/10.1016/j.applthermaleng.2015.03.065.

[31] N. A. M. Amin, F. Bruno, and M. Belusko, "Effective thermal conductivity for melting in PCM encapsulated in a sphere," *Appl. Energy,* vol. 122, pp. 280-287, 2014/06/01/ 2014, doi: https://doi.org/10.1016/j.apenergy.2014.01.073.

[32] H. Pointner *et al.*, "Computational efficiency in numerical modeling of high temperature latent heat storage: Comparison of selected software tools based on experimental data," *Appl. Energy,* vol. 161, pp. 337-348, 2016/01/01/ 2016, doi: https://doi.org/10.1016/j.apenergy.2015.10.020.

[33] W. Beyne and M. De Paepe, "Describing conduction dominated sensible thermal energy storage heat exchangers using thermal quadrupoles," presented at the Innovative solutions for thermal energy storage deployment, Lleida, 2023.

[34] W. Beyne, R. Tassenoy, M. Goderis, V. Van Riet, and M. De Paepe, "A predictive method for pipe in pipe, cylindrical modules and spherical packed bed latent thermal energy storage systems," *Journal of Energy Storage,* vol. 68, p. 107755, 2023.
[35] W. Beyne, R. Tassenoy, and M. De Paepe, "An approximate analytical solution for the movement of the phase change front in latent thermal energy storage heat exchangers," *Journal of Energy Storage,* vol. 57, p. 106132, 2023/01/01/ 2023, doi: https://doi.org/10.1016/j.est.2022.106132.
[36] W. Beyne, J. Degroote, and M. De Paepe, "Experimental validation of a design model for latent thermal energy storage extended with sensible heat," in *Journal of Physics: Conference Series*, 2024, vol. 2766, no. 1: IOP Publishing, p. 012217.
[37] C. Ding, Z. Niu, B. Li, D. Hong, Z. Zhang, and M. Yu, "Analytical modeling and thermal performance analysis of a flat plate latent heat storage unit," *Applied Thermal Engineering,* vol. 179, p. 115722, 2020/10/01/ 2020, doi: https://doi.org/10.1016/j.applthermaleng.2020.115722.
[38] W. Beyne, M. Goderis, V. Van Riet, and M. De Paepe, "Predicting the output of a latent thermal energy storage heat exchanger by decomposition into a series connection of heat exchangers with an analytical solution," in *International Heat Transfer Conference Digital Library*, 2023: Begel House Inc.
[39] M. Fiss, "Wärmespeichervorrichtung," Germany, 10/11/2012, 2012.
[40] M. Johnson, M. Fiss, T. Klemm, and M. Eck, "Test and analysis of a flat plate latent heat storage design," *Energy Procedia,* vol. 57, pp. 662-671, 2014.
[41] J. Vogel, J. Felbinger, and M. Johnson, "Natural convection in high temperature flat plate latent heat thermal energy storage systems," *Appl. Energy,* vol. 184, no. Supplement C, pp. 184-196, 2016/12/15/ 2016, doi: https://doi.org/10.1016/j.apenergy.2016.10.001.
[42] M. Johnson, M. Fiß, and T. Klemm, "Experimental testing of various heat transfer structures in a flat plate thermal energy

storage unit," in *AIP Conference Proceedings*, 2016, vol. 1734, no. 1: AIP Publishing.

[43] N. Bianco, A. Fragnito, M. Iasiello, G. M. Mauro, and L. Mongibello, "Multi-objective optimization of a phase change material-based shell-and-tube heat exchanger for cold thermal energy storage: experiments and numerical modeling," *Applied Thermal Engineering,* vol. 215, p. 119047, 2022/10/01/ 2022, doi: https://doi.org/10.1016/j.applthermaleng.2022.119047.

[44] D. Maillet, S. Andre, J. C. Batsale, A. Degiovanni, and C. Moyne, *Thermal quadrupoles: solving the heat equation through integral transforms*. John Wiley & Sons Incorporated, 2000.

[45] W. Beyne, M. De Paepe, and J. Degroote, "A sizing model for a tube in tube sensible thermal energy storage heat exchanger with solid storage material," *Journal of Energy Storage,* vol. 105, p. 114622, 2025.

[46] W. Beyne, M. Goderis, V. Van Riet, and M. De Paepe, "Predicting the output of a latent thermal energy storage heat exchanger by decomposition into a series connection of heat exchangers with an analytical solution," presented at the 17th international heat transfer conference, Cape Town, To be presented 14-18 august 2023, 2023.

[47] S. Kimura and A. Bejan, "The boundary layer natural convection regime in a rectangular cavity with uniform heat flux from the side," *Journal of heat transfer,* vol. 106, no. 1, pp. 98-103, 1984.

[48] Z. Wang, Y. Li, Y. Wang, and A. Li, "Stagewise melting heat transfer characteristics of phase change material in a vertically placed rectangular enclosure," *Journal of Energy Storage,* vol. 62, p. 106917, 2023/06/01/ 2023, doi: https://doi.org/10.1016/j.est.2023.106917.

[49] N. H. S. Tay, F. Bruno, and M. Belusko, "Experimental validation of a CFD model for tubes in a phase change thermal energy storage system," *Int. J. Heat Mass Transf.,* vol. 55, no. 4, pp. 574-585, 2012/01/31/ 2012, doi: https://doi.org/10.1016/j.ijheatmasstransfer.2011.10.054.

[50] B. Kiyak, H. F. Oztop, N. Biswas, and F. Selimefendigil, "Effects of geometrical configurations on melting and solidification processes in phase change materials," *Applied Thermal Engineering,* vol. 258, p. 124726, 2025.
[51] N. B. Khedher *et al.*, "Maximizing charging/discharging capabilities of horizontal shell-and-tube latent heat storage systems with innovative curved fin inserts," *Int. J. Heat Mass Transf.,* vol. 236, p. 126289, 2025.
[52] J. Taylor, *Introduction to error analysis, the study of uncertainties in physical measurements*. 1997.